Coupled atomistic–continuum simulations of nucleate boiling

Gabriele Gennari [a], Edward R. Smith [b], Gavin J. Pringle [c], Mirco Magnini [a],*

[a] *Department of Mechanical, Materials and Manufacturing Engineering, University of Nottingham, Nottingham, NG7 2RD, United Kingdom*
[b] *Department of Mechanical and Aerospace Engineering, Brunel University London, Uxbridge, UB8 3PH, United Kingdom*
[c] *EPCC, University of Edinburgh, Bayes Centre, Edinburgh, EH8 9BT, United Kingdom*

ARTICLE INFO

ABSTRACT

Boiling is a striking example of a multiscale process, where the dynamics of bubbles is governed by the interplay between the molecular interactions responsible for nucleation, and the macroscale hydrodynamic and thermal boundary layers. A complete description of this phenomenon requires coupling molecular- and continuum-scale fluid mechanics into a single modelling framework. This article presents a hybrid atomistic–continuum computational model for coupled simulations of nucleate boiling. A domain decomposition coupling method is utilised, where the near-wall region is solved by a Molecular Dynamics description, which handles nucleation and the moving contact lines, while the bulk flow region is solved by a continuum-scale description based on the Navier–Stokes equations. The latter employs a Volume Of Fluid method to track the evolution of the liquid–vapour interface and the interphase mass transfer is computed via the Hertz–Knudsen–Schrage relationship. Boiling of a Lennard-Jones fluid over a heated wall is simulated and the hybrid solution is validated against a fully molecular solution. The results obtained with the coupled framework in terms of time-dependent bubble volume, phase-change rates, bubble dynamics and evolution of the temperature field agree quantitatively with those achieved by a MD-only simulation. The coupled framework reproduces the bubble growth rate over time from nucleation until a bubble diameter of about 70 nm, demonstrating the accuracy and robustness of the coupling architecture. This also demonstrates that the fluid dynamics description based on the Navier–Stokes equations is capable of correctly capturing the main heat and mass transfer mechanisms responsible for bubble growth at the nanoscale. The proposed modelling framework paves the way towards multiscale simulations of boiling, where the necessary molecular-level physics is retained in a computational fluid dynamics solver.

1. Introduction

Nucleate boiling denotes the physical process where vapour bubbles are formed within a liquid phase upon heating above its equilibrium saturation temperature. Since it is more energetically favourable for bubbles to form over a solid wall rather than within the bulk liquid, bubbles typically nucleate in the proximity of solid walls and within geometrical imperfections left by the manufacturing process which may act as nucleation spots [1]. Boiling is widely exploited in science and engineering, in particular for the extraordinary energy transfer rates associated with the dissipation of the latent heat necessary to form the vapour bubbles, and is thus central to technological processes as diverse as power generation, water treatment and desalination, thermal control of compact devices, petroleum and chemical processing [2,3].

Boiling is a perfect example of a multiscale process. The process begins with the heterogeneous nucleation of nanometre bubbles owing to molecular-level interactions between the fluid and the hot surface, bubbles grow as liquid is being converted into vapour across the liquid–vapour interface, and they eventually depart from the hot surface when

they become sufficiently large to be mobilised either by buoyancy (mostly in pool boiling) or by the drag exerted by the flow of a fluid (flow boiling). Hence, the overall heat transfer associated with the process depends on parameters such as the bubble generation frequency, nucleation superheat and nucleation site density, macroscale behaviour that originates in molecular-level phenomena. At the same time, nucleation depends on the outer conditions of the system, for example the hydrodynamic and thermal boundary layers established on the heated wall. Therefore, there is a strong interplay between the nucleation physics occurring at nanometre and nanosecond scales, and the larger scale thermohydraulics where the external forces impacting bubble dynamics have scales of millimetres and milliseconds. The experimental methods for thermohydraulic diagnostics of boiling have advanced significantly over the past few years, providing spatiotemporally resolved two-dimensional temperatures maps of the heated wall during bubble growth via infrared thermography [4–6], measurement of micro-layer film thicknesses by laser interferometry [7], bubble growth rates via high-speed imaging [8], bulk velocity and temperature measurements via Particle Image Velocimetry and Laser Induced Fluorescence

---

* Corresponding author.
E-mail address: mirco.magnini@nottingham.ac.uk (M. Magnini).

conducted within the liquid surrounding the bubbles [9]. Nonetheless, even the most advanced experimental techniques are limited to spatial scales of micrometres and temporal scales of milliseconds, which are still insufficient to access many dynamics and localised aspects of the flow, and orders of magnitude larger than the nucleation itself. Numerical simulations have been increasingly used in the last decade to reveal essential aspects of boiling dynamics. Interface-resolved Computational Fluid Dynamics (CFD) simulations based on the solution of the Navier–Stokes equations have been widely used to study pool [10–12] and flow boiling [13–15]. However, the solution of the governing equations at the continuum-scale cannot capture the molecular interactions responsible for boiling onset, and thus CFD simulations require initial bubble seeds which are usually placed using random functions [16,17]. Furthermore, key microscale processes such as the liquid–vapour interphase mass transfer occurring during phase-change, the dynamics of the triple contact line at the wall, the stability and rupture of thin liquid films, all rely on thermodynamic models that require input from molecular-level information, e.g. the evaporation and condensation coefficients in the Hertz–Knudsen–Schrage equation for phase-change mass transfer [18]. Molecular Dynamics (MD) is the most fundamental approach to simulate bubble nucleation from first principles and a number of studies on pool boiling were conducted in recent years [19,20], however, MD can only achieve nanosecond and nanometre scales due to the computational cost of modelling the kinetics of millions of interacting molecules.

Hybrid MD-CFD approaches started to appear recently, in an attempt to introduce molecular details into engineering-scale CFD simulations at reduced computational cost [21]. The simplest MD-CFD coupling can be achieved by embedding the results of sequentially or concurrently run MD simulations into a continuum-scale framework to provide missing information, a technique known as *heterogeneous coupling*. For example, Zhang et al. [22] performed a series of MD simulations of droplet spreading over a solid surface to set advancing, receding contact angles and slip length into a CFD model based on the Volume Of Fluid method (VOF) [23], which was able to reproduce the droplet dynamics obtained via MD down to nanometre-sized droplets. Another approach is *domain decomposition coupling*, where MD and CFD actually run simultaneously and resolve different regions of the computational domain, with flux or state properties being directly exchanged in an overlap region, without intermediate models [24,25]. Typically, MD is limited to regions of the domain where molecular-level interactions are important, e.g. near a fluid–fluid or fluid–wall interface, while the CFD resolves the fluid dynamics in the fluid bulk. This technique is well established for wall-bounded single-phase flows and significant speed-up was reported for Couette flow simulations with domains of about 100 nm [26–29], compared to MD-only runs. As such, domain decomposition coupling is an ideal technique to dynamically link molecular-scale bubble nucleation and continuum-scale fluid mechanics. However, very few attempts have been made to apply this methodology to multiphase flows. One of the first works on coupling [30] combined MD with a finite-element solver to model the moving contact line problem of a meniscus separating gas and liquid within a nanochannel, using the full MD solution of the same problem as a validation benchmark. Wu et al. [31] adopted it to simulate the unsteady dynamics of a droplet of 60 nm radius spreading over a solid wall. The MD resolved the contact line region and a finite-volume method was used to resolve the far field region, modelled by means of the incompressible Navier–Stokes equations for a Newtonian fluid. A similar modelling framework, but with the VOF method adopted to capture the liquid–gas interface dynamics in the CFD model, was recently utilised by Saha and Das [32] to study the motion of nanodroplets on surfaces with varying hydrophilicity. Zhang et al. [22] coupled MD and a CFD model based on the incompressible Navier–Stokes equations to study nucleate boiling on a structured surface. The MD data near the coupled boundary were used to set velocity and temperature boundary conditions in the CFD, while the CFD solution was used to impose

constraints on the MD velocity. The bubble nucleated in the MD domain and, to avoid the complexity of modelling the transition of the bubble from the MD to the CFD, the coupled boundary shifted upward during the bubble growth, so that the CFD always modelled a single-phase flow. Mao et al. [33] also modelled nucleate boiling using MD coupled with a finite-volume method solving the incompressible flow equations, but using a VOF method in order for the CFD model to handle the liquid–vapour interface dynamics as the bubble entered the CFD region. The phase-change rate in the CFD was calculated proportional to the heat flux at the interface, according to continuum-scale heat transfer principles. The coupled framework was showcased by simulating boiling over nanoscale defects, although neither verification of the coupling consistency nor validation versus MD-only results were presented. In summary, to date only very few attempts have been made to model boiling with a hybrid atomistic–continuum framework based on domain decomposition, and the few studies available did not exhibit any rigorous validation versus benchmark data. A validated coupled MD-CFD framework using domain decomposition holds potential towards achieving true multiscale simulations of boiling.

In this article, a novel coupled framework for MD-CFD hybrid simulations of nucleate boiling is presented and validated against a fully molecular solution for the first time. The MD model is based on a Lennard-Jones fluid. The CFD model employs a VOF method to resolve the liquid–vapour interface dynamics and a phase-change model based on the Hertz–Knudsen–Schrage equation. A one-way domain decomposition coupling method is adopted, with the time-dependent MD data used to set the boundary conditions for phase fraction, velocity and temperature in the CFD model. The coupled solver is utilised to simulate nucleate boiling over a surface defect and the results in terms of time-dependent bubble volume, phase-change rates, bubble dynamics and evolution of the temperature field, exhibit quantitative agreement with those achieved by a MD-only simulation. The coupled framework is capable of reproducing the bubble growth rate over time from nucleation until a bubble size of about 70 nm, demonstrating the accuracy and robustness of the coupling architecture, and that the fluid dynamics description based on the Navier–Stokes equations is capable of correctly capturing the main heat and mass transfer mechanisms responsible for bubble growth at the nanoscale. Moreover, the good agreement of near-interface temperatures and phase-change rates between MD and CFD further confirms the validity of the Hertz–Knudsen–Schrage equation to represent evaporation and condensation phase-change over curved and dynamic interfaces at the nanoscale, which was to date demonstrated only for steady-state mass transfer processes and flat interfaces [34]. The entire numerical framework is open-source and publicly available on Github (github.com/Crompulence/CPL_APP_OPENFOAM).

The rest of this article is organised as follows: the coupled MD-CFD framework is described in Section 2; the setup of the nucleate boiling simulation is introduced in Section 3; the results of the simulations are presented in Section 4; in Section 5, perspectives for multiscale simulations are discussed; the conclusions of this work are summarised in the final Section 6.

2. Coupled numerical framework

The numerical framework is composed of an MD solver and a CFD solver that run concurrently, each solving part of the domain. At the interface, there is an overlapping region to allow a physical transition from molecular to continuum description. A schematic representation of the setup is displayed in Fig. 1. The MD solver models the heated wall and a thin region of fluid above it. The actual MD simulation goes far beyond the coupled boundary, with the molecules above the point of coupling acting as a buffer, a large liquid region to allow the nucleated vapour bubble to grow without being affected by the top boundary of the MD domain, and a large layer of vapour on top of the liquid phase. This vapour region prevents pressure build-up within
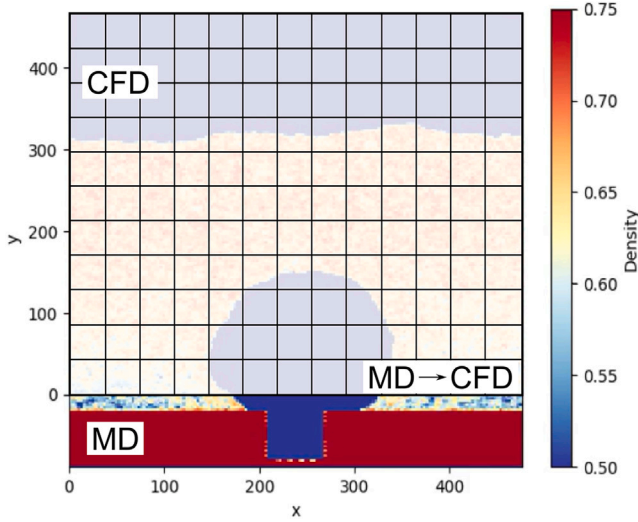
Fig. 1. Schematic of the coupled MD-CFD setup. The CFD domain partially overlaps the MD domain. The coupled boundary where MD time-dependent fields of density, velocity and temperature are passed to CFD is positioned above the heated wall and within the fluid region, at $y = 0$. The unit length is approximately 0.34×10^{-9} m; useful conversion factors from MD to SI units are reported in Table 1. The CFD grid shown in the image above is illustrative.

the MD domain as the bubble grows. The top boundary is then set as a specular wall. The CFD domain incorporates the fluidic region but does not include the heated wall, which is handled exclusively by MD. The bottom boundary of the CFD domain is obtained from the average of the MD field at a position slightly above the wall–fluid interface. In this way, the bubble nucleation and contact lines do not need to be resolved by the CFD model. On this boundary, the CFD model receives time-dependent density, velocity and temperature data from MD, which are imposed as Dirichlet boundary conditions to the continuum governing equations. Note that the origin $y = 0$ is chosen to be coincident with the coupled boundary, so the MD region is negative y and the CFD positive. The coupling is only one-way in this work, sending information from MD to CFD only. This greatly simplifies the coupling architecture, which does not need MD constraints and atoms addition or deletion [22,33]. Any MD data above the coupled boundary is not used in the CFD solver and thus the MD density contours in Fig. 1 are displayed in slight transparency for $y > 0$. However, this data will be useful to compare the results of the MD-only simulation, regarded as the exact solution, with those of the coupled framework. Details of the geometrical parameters of the simulation and of the boundary conditions set to both MD and CFD are provided in Section 3. In the subsections below, the MD, CFD and coupling method are described in detail.

2.1. Molecular dynamics (MD) solver

In order to focus on the fluid dynamics instead of chemistry, the simple and widely used Lennard-Jones potential is applied for the molecular dynamics:

$$U(r_{ij}) = 4\epsilon \left[\left(\frac{\sigma}{r_{ij}} \right)^{12} - \left(\frac{\sigma}{r_{ij}} \right)^6 \right] - 4\epsilon \left[\left(\frac{\sigma}{r_c} \right)^{12} - \left(\frac{\sigma}{r_c} \right)^6 \right] \quad (1)$$

where U is the potential energy, ϵ is the potential well depth, σ is the molecular diameter, r_{ij} is the distance between molecules i and j, and r_c is the cutoff distance. All numbers are given in reduced Lennard-Jones units, normalised by $\sigma = 0.34$ nm and $\epsilon = 120 k_B$ where k_B is the Boltzmann constant. The molecular dynamics simulations are performed using the *flowmol* code [35], which has been validated in previous publications. This includes energy conservation

and comparison to the radial distribution functions which validate the code at the lowest level, comparing the molecular structure to neutron scattering experiments, as well as the phase change of the MD model through comparison to results from NIST [35]. For the fluid dynamics behaviour, a comparison to the unsteady Couette flow analytical solution was also undertaken [36]. The MD model has been shown to match experimentally measured values of surface tension and viscosity of liquid Argon [37], and to capture the temperature-dependent trend of the thermal conductivity of a Lennard-Jones fluid in agreement with benchmark data [38]. Previous work has shown that a cutoff of $r_c = 4.5$ is required to give surface tension which matches experiments [37]. However, here the cutoff is set to $r_c = 2.5$ to allow multiphase effects but to keep simulation times reasonable.

Averages of density, velocity, temperature and volume averaged pressure tensor [39] are taken in the MD simulation, by decomposing the MD domain into control volumes. The density and momentum in a control volume are given as follows:

$$\int_V \rho dV = \sum_{i=1}^{N} \langle m_i \vartheta_i \rangle \quad (2)$$

$$\int_V \rho \boldsymbol{u} dV = \sum_{i=1}^{N} \langle m_i \dot{\boldsymbol{r}}_i \vartheta_i \rangle \quad (3)$$

where ϑ_i is the integral of the Irving and Kirkwood [40] Dirac delta function over a volume [36], m_i is the mass of molecule i, $\dot{\boldsymbol{r}}_i$ is its velocity and the $\langle \rangle$ operator denotes averaging over time. The temperature is then:

$$\int_V T dV = \sum_{i=1}^{N} \langle m_i \boldsymbol{v}_i^2 \vartheta_i \rangle \quad (4)$$

where $\boldsymbol{v}_i = \dot{\boldsymbol{r}}_i - \boldsymbol{u}$ is the so called peculiar velocity, with the streaming velocity subtracted to give just the thermal fluctuations [41,42]. The local volume-averaged pressure tensor [43] is given by:

$$\int_V \boldsymbol{\Pi} dV = \sum_{i=1}^{N} \left\langle m_i \boldsymbol{v}_i \boldsymbol{v}_i \vartheta_i + \sum_{j \neq i}^{N} \boldsymbol{f}_{ij} \boldsymbol{r}_{ij} \ell_{ij} \right\rangle \quad (5)$$

where ℓ_{ij} takes the fraction of the interaction force $\boldsymbol{f}_{ij}$ inside a volume between molecule i and j separated by vector $\boldsymbol{r}_{ij}$. The pressure tensor $\boldsymbol{\Pi}$ can be equated to the right hand side of the Navier–Stokes equation given below in Eq. (8), so, $\boldsymbol{\Pi} = -p\boldsymbol{I} + \mu[(\nabla \boldsymbol{u}) + (\nabla \boldsymbol{u})^T]$ where $\boldsymbol{I}$ is the identity matrix. The angular brackets denote an average over time with 100 samples taken every 25 time-steps, so a MD snapshot is written every 2500 time-steps.

2.2. Computational fluid dynamics (CFD) solver

The CFD model is based on the solution of the continuum Navier–Stokes equations as implemented in the opensource toolbox OpenFOAM v2106. The liquid–vapour two-phase boiling flow is simulated by means of a Volume Of Fluid [23] interface capturing method, using our self-developed library boilingFoam [44], which was extensively validated in previous articles against theoretical benchmarks and experimental data [15,45]. Of particular relevance to the present work is the validation versus experimental pool boiling data performed by Municchi et al. [45]. The pool boiling of saturated water at atmospheric pressure over a heated wall was simulated and the results in terms of time-dependent bubble volume and heater temperature were compared to the experimental measurements of Bucci [46]. The experimental and numerical results agreed within 4% for the heater temperature and 13% for the bubble volume; additional details are included in the Supplementary Content document (Section 1).

The CFD library solves the partial differential equations for the VOF phase fraction, continuity, momentum and energy transport for an incompressible flow and Newtonian fluid, formulated as follows:

$$\frac{\partial \alpha}{\partial t} + \nabla \cdot (\alpha \boldsymbol{u}) = \frac{\dot{\rho}}{\rho} \alpha \quad (6)$$

$$\nabla \cdot \boldsymbol{u} = \frac{\dot{\rho}}{\rho} \tag{7}$$

$$\frac{\partial(\rho\boldsymbol{u})}{\partial t} + \nabla \cdot (\rho\boldsymbol{u}\boldsymbol{u}) = -\nabla p + \nabla \cdot \mu\left[(\nabla\boldsymbol{u}) + (\nabla\boldsymbol{u})^T\right] + \boldsymbol{F}_s \tag{8}$$

$$\frac{\partial(\rho c_p T)}{\partial t} + \nabla \cdot (\rho c_p \boldsymbol{u} T) = \nabla \cdot (\lambda \nabla T) + \dot{h} \tag{9}$$

where α denotes the liquid VOF phase fraction, $\boldsymbol{u}$ the fluid velocity, $\dot{\rho}$ the volumetric mass source due to phase-change, ρ the mixture fluid density, t the time, p the pressure, μ the dynamic viscosity, $\boldsymbol{F}_s$ the surface tension force vector, T the temperature, c_p the constant pressure specific heat, λ the thermal conductivity, and $\dot{h}$ is the enthalpy source due to phase-change. The gravitational force is not included in the momentum equation as its effect is negligible at the spatial scale considered in this work. The VOF phase fraction represents the fraction of the cell volume occupied by liquid and is $\alpha = 1$ in a cell filled with liquid, $\alpha = 0$ in a cell filled with vapour, and $0 < \alpha < 1$ in an interface cell. All fluid properties are evaluated as α-weighted mixtures of liquid and vapour properties as is customary for the VOF method, for example the mixture fluid density is calculated as:

$$\rho = \rho_l \alpha + \rho_v(1 - \alpha) \tag{10}$$

where ρ_l and ρ_v are the liquid and vapour specific densities. In the CFD model, all liquid- and vapour-specific properties are considered constant. The surface tension force is implemented using the Continuum Surface Force method [47]:

$$\boldsymbol{F}_s = \beta\kappa|\nabla\alpha| \tag{11}$$

where β is the surface tension coefficient, which is considered constant, and κ is the local interface curvature which is evaluated based on gradients of the phase fraction as $\kappa = -\nabla \cdot (\nabla\alpha/|\nabla\alpha|)$. The volumetric mass source due to phase-change is calculated as:

$$\dot{\rho} = \dot{m}|\nabla\alpha|, \quad \dot{m} = \frac{2\gamma}{2-\gamma}\left(\frac{M}{2\pi R_g}\right)^{1/2}\frac{\rho_v h_{lv}(T_{lv} - T_{sat})}{T_{sat}^{3/2}} \tag{12}$$

where $\dot{m}$ is the interfacial mass flux evaluated using the Hertz–Knudsen–Schrage relationship [1] with the linearisation proposed by Tanasawa [48], γ is the accommodation coefficient, h_{lv} is the vaporisation latent heat, M is the molecular weight of the fluid, R_g the universal gas constant, T_{lv} is the temperature at the liquid–vapour interface, and T_{sat} the saturation temperature of the fluid. During the evaporation process, the molecules that enter the bulk vapour region may be either molecules coming from the evaporating liquid phase, or molecules that from the vapour region strike the interface but do not condense, thus being reflected towards the bulk vapour; the accommodation coefficient is defined as the fraction of the molecules that enter the bulk vapour region due to liquid vaporisation [1], and thus must be between 0 and 1. Note that, in Eq. (12), positive values of the mass flux identify liquid-to-vapour phase-change (evaporation) whereas negative values identify vapour-to-liquid phase-change (condensation). The enthalpy source term, $\dot{h}$ in Eq. (9), removes the latent heat of the fluid and is calculated from the volumetric source term as $\dot{h} = -\dot{\rho}h_{lv}$. This evaporation model has been extensively used in the CFD practice and has been widely validated against theoretical and experimental benchmarks [10,15,49].

OpenFOAM solves the governing equations with a finite-volume method on a collocated grid arrangement. The VOF phase fraction Eq. (6) is discretised with a first-order time-explicit scheme based on the MULES (Multidimensional Universal Limiter for Explicit Solution) algorithm [50], whereas the remaining equations are integrated in time with a first-order implicit scheme. The divergence operators are discretised using second-order TVD (Total Variation Diminishing) schemes [51], whereas Laplacian operators are discretised with central finite-differences. The PISO (Pressure Implicit Splitting of Operators) algorithm [52] is utilised to iteratively update pressures and velocities

within each time-step. The residuals thresholds for the iterative solution of the flow equations are set to 10^{-7} for the velocity, 10^{-8} for the pressure and the volume fraction, and 10^{-10} for the temperature. The smoothing procedure proposed by Hardt and Wondra [49] is adopted to distribute the volumetric mass source $\dot{\rho}$ over a few computational cells across the interface and prevent numerical instabilities. This strategy is especially beneficial near the coupled boundary, to damp down local spikes in evaporation rates induced by fluctuations in the MD temperature field.

2.3. MD-CFD coupling

The spatial coupling is one-way, from MD to CFD, and is realised across the bottom CFD boundary as indicated in Fig. 1. The MD fields of density, velocity and temperature are averaged as time elapses in the MD simulation both in time and space as explained in Section 2.1. The average values of each field are then interpolated onto the boundary faces of the coupled (bottom) CFD boundary and imposed as Dirichlet boundary conditions for the related equations. This operation is straightforward for velocity and temperature as their partial differential equations, Eqs. (8) and (9), are directly solved in the CFD model. However, since the CFD solver is incompressible, no equation for density is solved and the density data from MD must be converted into phase fraction data, to be used as boundary conditions for the VOF fraction Eq. (6). This is accomplished by thresholding the MD density data based on a representative interface density value ρ_c taken as an average of liquid and vapour specific densities, $\rho_c = 0.5(\rho_l^{CFD} + \rho_v^{CFD})$, as follows:

$$\alpha = \begin{cases} 1, & \text{if } \rho^{MD} > \rho_c \\ 0, & \text{if } \rho^{MD} < \rho_c \end{cases} \tag{13}$$

where ρ^{MD} is the density in the MD control volume and ρ_l^{CFD}, ρ_v^{CFD} are the liquid and vapour densities set in the CFD simulation. Hence, the fluid entering the CFD domain through the coupled boundary is either pure liquid ($\alpha = 1$) or pure vapour ($\alpha = 0$). Another possibility would be to allow intermediate values of α by calculating the phase fraction from MD density values using the definition of mixture density in the CFD as written in Eq. (10), and thus replacing Eq. (13) with $\alpha = (\rho^{MD} - \rho_v^{CFD})/(\rho_l^{CFD} - \rho_v^{CFD})$. However, due to the density fluctuations in the MD, the resulting values of α along the coupled boundary vary between $0 < \alpha < 1$ and are highly nonuniform. In our tests, this generates gradients of volume fraction that would be erroneously interpreted as liquid–vapour interfaces by the phase-change model, which during the compute of phase-change rates via Eq. (12) result in nonphysical bubble nucleation along the coupled boundary. In addition to the phase fraction, both velocity from Eq. (3) divided by Eq. (2) and temperature from Eq. (4) are obtained from the MD and set as boundary conditions for the CFD solver. It would also be possible to directly set pressure from the MD, Eq. (5), but this is often prohibitively noisy [53] and the use of an incompressible CFD solver makes this unnecessary.

The temporal coupling between the MD and CFD solutions is intermittent [54]. The MD and CFD solutions evolve synchronously, i.e. over the same timeline, but the time-step of the MD simulation is orders of magnitude smaller than that of the CFD, as the limits on the MD time-step set by the molecular scale dynamics are much stricter than the CFL limit or capillary time-step [55] limit in the CFD solver. Therefore, the CFD boundary conditions at the coupled boundary are updated every $N_{MD\rightarrow CFD}$ MD time-steps as detailed in Section 3.2.

The overall coupling information exchange for the MD and CFD solutions is based on the CPL library developed by Smith et al. [56]. CPL library is inspired by the message passing interface (MPI) [57] providing a platform independent library which can link into existing codes to facilitate domain decomposition coupling. Both codes run independently, with all information sent and received using CPL_send and CPL_recv functions which are added in to the appropriate part of both coupled solvers. For OpenFOAM, these are added to a new
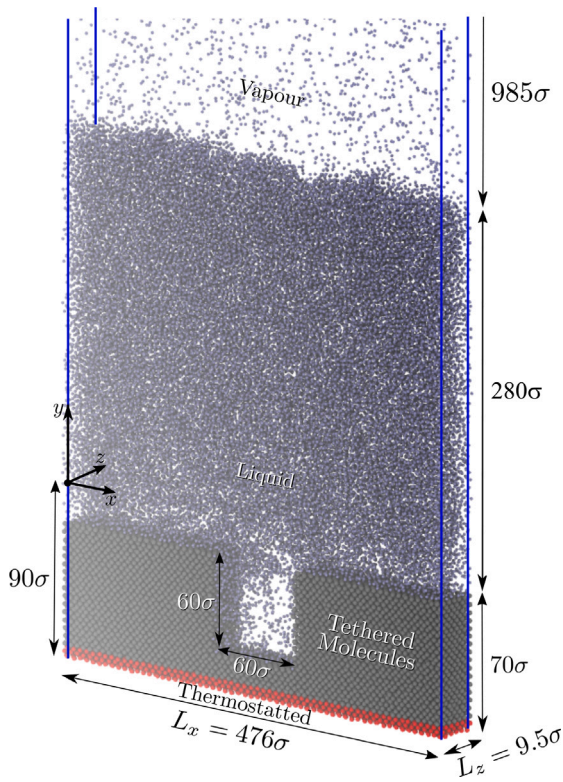
Fig. 2. Schematic of the Molecular Dynamics setup, wall geometry and domain extensions. The reference length σ is approximately $\sigma \approx 0.34 \times 10^{-9}$ m. The snapshot is taken from the MD solution. The horizontal $x-z$ plane at $y=0$, located 20σ above the top surface of the solid wall, coincides with the coupled CFD boundary.

boundary condition which receives time-dependent MD data during runtime and sets the bottom boundary conditions for the CFD fields of VOF volume fraction, velocity and temperature as explained above. The other main responsibility of CPL library is to setup the coupled run using CPL_init, which either merges independent MPI communicators or splits them if using a single MPI_COMM_WORLD. Then, the mapping between the two codes is established by CPL_setup (CFD and MD versions) where the overlap of the two domains is used to determine where to send data. An example of a two-way MD-CFD domain decomposition coupling realised for a single-phase Couette flow is included in the Supplementary Content document (Section 2). In the one-way coupling architecture utilised in the work presented in this article, the MD code is replaced by a Python script that reads data written to file by a previous run large-scale MD simulation. The data exchange is in exactly the same format that the MD code would send, and the data from the CFD code which would be used to accelerate the MD field is received but not used in the Python script. This allows us to focus on developing and testing the CFD part of the coupling with input from MD as the boundaries, removing the computational cost of the MD and the complexity of two-way coupling. Coupling two non-linear solvers has the potential to give divergent results, so this removes some of this complexity while capturing the essential physics, i.e. the bubble nucleation and early time growth, to check a fully coupled MD-CFD configuration agrees with the pure MD case.

3. Simulation setup

3.1. MD setup

A schematic representation of the MD simulated system is shown in Fig. 2. It consists of a system of $N = 1,222,652$ Lennard-Jones molecules contained in a box of size $L_x = 476\sigma$ by $L_y = 1270\sigma$ by $L_z = 9.5\sigma$, where

the z dimension is chosen to be a minimal thickness so the simulation is pseudo 2D. In this work, all units are expressed in reduced MD units; the conversion factors to SI units are reported in Table 1. Since the Lennard-Jones potential yields a good approximation of intermolecular interactions for simple substances such as Argon [58], Table 1 includes also quantitative values of the conversion factors calculated in the case of an Argon-like system. The solid wall at the bottom of the domain is composed of a 70σ layer of tethered molecules and a square cavity of depth and width of 60σ is placed at the centre of the wall to induce the nucleation of the bubble. Walls are tethered to the FCC lattice sites with harmonic spring constant $k_1 = 150$. The simulation is initialised with a wall density set to $\rho_w = 1.0$, the liquid density $\rho_l = 0.75$, and vapour density is $\rho_v = 0.02$. These different regions of densities are achieved by setting up an FCC lattice of density ρ_w everywhere and deleting molecules at random until the target density ρ_l or ρ_v is achieved. The top boundary in y is set as a specular wall, which reflects the molecules with equal and opposite y momentum, and periodic boundaries are used in x and z. The liquid phase initially fills up to the half way mark of the domain with a coexisting vapour phase filling up the top 635σ of the domain. An equilibration with the Nosè–Hoover thermostat applied to all molecules in the system is then run for 1 million time-steps (MD time-step $\Delta t = 0.005$), until a homogeneous temperature of $T = 0.9$ is reached and the system has stopped changing phases with average fluid pressure $p = 0.032$. The liquid region remains attached to the solid wall, but is of thickness $\sim 270\sigma$ by the end of equilibration with density $\rho_l = 0.68$. Vapour covers a region of thickness 930σ up to the domain top and has density of $\rho_v = 0.0175$. These density and pressure values at equilibrium are consistent with those reported in the literature; for example, Trokhymchuk and Alejandre [59] reviewed the available data for Lennard-Jones fluids and documented liquid densities of $0.66-0.67$ and equilibrium pressures of $p \approx 0.03$ for $T = 0.9$, when the same cutoff radius $r_c = 2.5$ was used.

The equilibrated system is then used as an initial condition for the main boiling run. A Nosè–Hoover thermostatting region is applied to only a layer of tethered molecules of thickness 6σ underneath the solid wall (red molecules in Fig. 2), to model external heating to a setpoint temperature of 1.05; this corresponds to a temperature of 126 K in SI units, using the conversion factor reported in Table 1. The wall–fluid interaction is chosen to be $\epsilon_{ij,w} = 1$ (same as fluid–fluid), corresponding to a hydrophilic wall [19]. Outside of this thermostatted region, the remaining molecules are not thermostatted or barostatted. This lack of thermal or pressure control is to prevent unexpected damping of the velocity and growth of the bubble during the boiling process. The large vapour region at the domain top acts as a buffer so that the system does not change in pressure considerably during the simulation, from $p = 0.032$ at the start to $p = 0.0345$ when the bubble has reached a diameter of 175σ.

The MD simulation is run using parallel decomposition, through the message passing interface (MPI) [57], to solve on 40 cores in parallel. A time-step of $\Delta t = 0.005$ is used with a leap frog integrator. The end time of the simulation is $t = 6800$, which corresponds to about 15 ns. In order to compute the spatial averages indicated in Section 2.1, the MD domain is split into a grid of control volumes, with 160 by 453 by 3 cells in x, y and z respectively.

3.2. CFD and coupling setup

The CFD domain is a square box of $460\sigma \times 460\sigma \times 9.5\sigma$, see schematic in Fig. 1. The bottom boundary of the CFD domain is positioned 20σ, i.e. $6.8\,\mathrm{nm}$, above the fluid–wall interface in the MD and coincides with the origin of the coordinate system. Dirichlet boundary conditions for VOF phase fraction, velocity and temperature are imposed on this boundary, with time-dependent data received from the MD simulation as explained in Section 2.3. Pressure is not coupled and thus a zero-gradient boundary condition is set for the solution of the Poisson pressure equation. The top boundary is set as

Table 1

Conversion factors from Lennard-Jones (LJ) to International System (SI) units. The rightmost column reports the values of the conversion factors when considering an Argon-like system of molar mass of $39.95\,\mathrm{g/mol}$, which divided by the Avogadro constant yields a mass conversion factor of $m = 6.634 \times 10^{-26}\,\mathrm{kg}$. The conversion factors τ and ω are introduced for time and temperature, respectively.

Unit	LJ-to-SI conversion	Conversion factor	Value (Argon-like system)
Length	$L^{SI} = \sigma L^{LJ}$	σ	0.34×10^{-9} m
Mass	$M^{SI} = m M^{LJ}$	m	6.634×10^{-26} kg
Time	$t^{SI} = \tau t^{LJ}$	$\tau \equiv (m\sigma^2/\epsilon)^{1/2}$	2.15×10^{-12} s
Temperature	$T^{SI} = \omega T^{LJ}$	$\omega \equiv \epsilon/k_B$	120 K

Table 2

Thermophysical properties used in the CFD model. The values are set in reduced Lennard-Jones units; their corresponding values in SI units are included below within brackets, and are obtained by multiplying the values in LJ units by the conversion factors included in the first row of the table. Values and definitions of the conversion factors are reported in Table 1. The properties of the fluid in the CFD simulation, except for the liquid and vapour densities, are taken from the NIST website by considering saturated Argon at $T_{sat} = 108\,\mathrm{K}$. Liquid and vapour densities are set to match the values calculated from the MD simulation.

	$\rho\,(\mathrm{kg\,m^{-3}})$	$\mu\,(\mathrm{kg\,m^{-1}\,s^{-1}})$	$\lambda\,(\mathrm{W\,m^{-1}\,K^{-1}})$	$c_p\,(\mathrm{J\,kg^{-1}\,K^{-1}})$	$\beta\,(\mathrm{N\,m^{-1}})$	$h_{lv}\,(\mathrm{J\,kg^{-1}})$
LJ-to-SI	m/σ^3	$m/(\sigma\tau)$	$m\sigma/(\omega\tau^3)$	$\sigma^2/(\omega\tau^2)$	m/τ^2	m^2/τ^2
Liquid	0.68 (1148)	1.63 (0.000148)	5.23 (0.099)	5.77 (1202)	0.53 (0.0076)	5.69 (142254)
Vapour	0.05 (84)	0.0992 (0.000009)	0.4 (0.0075)	3.32 (691)		

an open boundary, by imposing zero-gradient conditions to velocity, temperature and VOF fraction, with a constant pressure. The CFD solver is incompressible, and thus the reference pressure value is unimportant. Since the open boundary allows the fluid to exit the domain as the bubble grows, the CFD domain is initially filled with liquid and there is no need to initialise a buffer vapour layer as done for the MD. The side ($x = 0, x = L_x$) and front/back ($z = 0, z = L_z$) boundaries of the domain are periodic, to match the MD setup. The CFD mesh is a structured orthogonal mesh with $160 \times 60 \times 3$ cells along the three coordinate directions. A grid independence analysis which confirms that the results have very little sensitivity to the mesh used is provided in Appendix A.

The liquid density in the CFD model is set equal to the value extracted from the equilibrated MD simulation, $\rho_l^{CFD} = 0.68$. Although the vapour density from the equilibrated MD simulation is $\rho_v = 0.0175$ as reported in the previous section, this value is calculated as an average density for the vapour layer on top of the liquid and, as it will be discussed in Section 4.1, does not necessarily correspond to the vapour density within the bubble. Hence, the vapour density in the CFD simulation is set to $\rho_v^{CFD} = 0.05$, which is evaluated from the MD boiling simulation as explained in Section 4.1. The other fluid thermophysical properties are not available from the MD simulation. By assuming that the Lennard-Jones fluid is a good approximation of Argon, the properties of saturated Argon at a temperature of $T = 108\,\mathrm{K}$, corresponding to the MD temperature of $T = 0.9$ at which the system is equilibrated prior to the boiling run, are utilised; the values are taken from the NIST database (nist.gov) and are listed in Table 2 in both Lennard-Jones and SI units. Note that a slight deviation of the thermophysical properties of the Lennard-Jones fluid from those of Argon is expected, owing to the choice of the cutoff radius [59] and to the limitations of the Lennard-Jones model. For example, the liquid density of saturated Argon at $T = 108\,\mathrm{K}$ from NIST is $1258\,\mathrm{kg/m^3}$ and 0.74 in reduced MD units, i.e. about 10% higher than the value measured in the present MD simulation. Smith et al. [37,38] calculated the dynamic viscosity, surface tension and thermal conductivity from non-equilibrium MD simulations of a Lennard-Jones system and reported values of $\mu = 1.3$, $\beta = 0.6 - 0.7$ and $\lambda = 4.5$ at $T \approx 0.9$; these compare quite well with the NIST data for Argon in Table 2, with a maximum deviation of 20% on viscosity. The CFD phase-change model, Eq. (12), requires knowledge of the saturation temperature of the fluid and of the accommodation coefficient, which are not readily available from the MD boiling simulation. Therefore, their values will be object of a parametric analysis in Section 4.2.3. The molecular weight in Eq. (12) is set to that of Argon. Note that the hybrid MD-CFD formulation where

MD handles the wall and near-wall region does not require for any contact line or contact angle model, because the contact line is outside the CFD domain. Thus, the contact angle does not need to be set in the CFD model and the contact line physics results exclusively from the molecular dynamics.

As an initial condition, the CFD domain is filled with liquid. The initial temperature of the liquid is set to the liquid average temperature resulting from the MD simulation at the end of the equilibration stage, which is $T = 0.882$. The CFD time-step must be sufficiently small to satisfy the capillary time-step restriction for flows with surface tension, $\Delta t^{CFD} < \sqrt{(\rho_l + \rho_v)\Delta^3/(4\pi\beta)}$ [55], with Δ being the mesh size, and is thus set to $\Delta t^{CFD} = 1.25$. The fields of density, velocity and temperature to be used as CFD boundary conditions at the coupled boundary are updated every $N_{MD\to CFD} = 2500$ MD time-steps, which are necessary to calculate temporally averaged MD fields as explained in Section 2.1. This corresponds to a time interval of 12.5 in MD units. Since the CFD time-step is 1.25, the boundary conditions in the CFD are updated every 10 CFD time-steps.

The computational cost of the CFD simulation is very small compared to that of MD and the overhead induced by the coupling is negligible. The CFD simulation is run on UK's national tier-1 supercomputer ARCHER2 using two computational cores, and it takes only a few minutes to reach the end time of $t = 6800$, chosen to match that of the MD-only simulation.

4. Results

The results of the simulations are presented below, with Section 4.1 first illustrating the results of the MD-only simulation and Section 4.2 discussing the results of the coupled simulations.

4.1. MD-only simulation

The MD simulation begins with the fluid and the solid wall initially at a uniform temperature of about 0.9, heated up over time from the bottom of the solid wall which is maintained at a constant temperature of 1.05 (126 K in SI units). Fig. 3 shows the evolution of density (Fig. 3a–c) and temperature (Fig. 3d-f) fields at different times. Three different zones are clearly distinguishable from the contours of density: a bottom region with a large density value ($\rho > 0.75$) corresponding to the solid wall with a central cavity, a layer of liquid ($\rho \approx 0.7$) adjacent to the wall and a region of vapour ($\rho \approx 0.02$, below the minimum value of the colour bar) at the top of the domain.
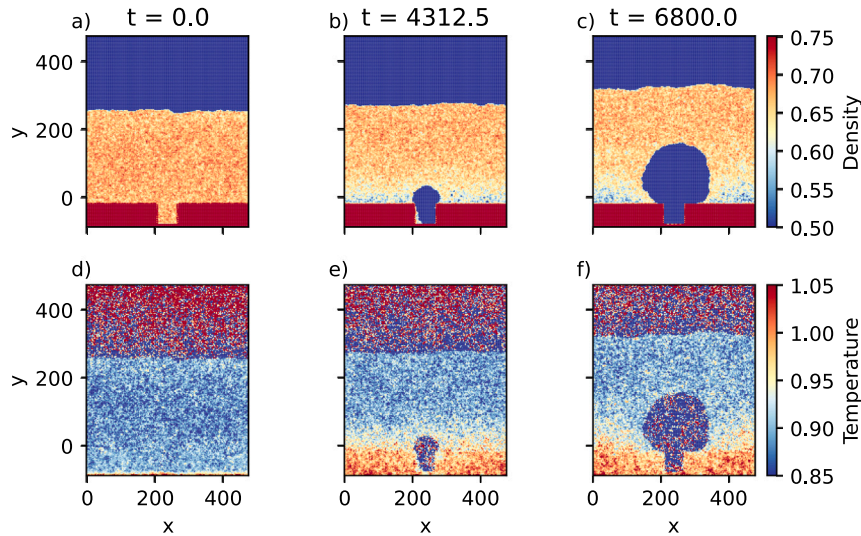
Fig. 3. Contours of density (a,b,c) and temperature (d,e,f) from the MD-only simulation at different times. The bottom wall is initially in contact with only liquid (a) at uniform temperature (d). As time elapses, a thermal boundary layer diffuses into the liquid region above the wall (e,f), whilst a vapour bubble nucleates within the cavity at $t \approx 4000$ (b) and grows as more heat is released into the system (c).

At the onset of the simulation, the solid wall quickly heats up from the bottom boundary and reaches a steady average temperature of approximately $T \approx 1.05$. The heat generated at the wall then diffuses into the adjacent layer of liquid and a thermal boundary layer forms on top of the wall and within the cavity, which exhibits the highest liquid temperature and thus constitutes a preferential nucleation spot. During this initial stage where a bubble has not yet formed, the heat transfer mechanism within the fluid is single-phase heat conduction and can be well described by a heat transfer model based on the Fourier law as demonstrated by Lavino et al. [19]. A certain amount of time is necessary before the liquid molecules absorb enough thermal energy to overcome the energy barrier to nucleation so that a stable vapour region can form. Owing to the hydrophilic wall, it is expected that the bubble first nucleates inside the cavity [19,20]. A prediction of the nucleation temperature can be obtained by considering the Young–Laplace and Clausius–Clapeyron equations. For a stable embryo bubble to exist inside the cavity, the lowest equilibrium vapour pressure is achieved when the embryo size coincides with the cavity size, i.e. a circular bubble of radius of $R_b = 30\sigma$ (10 nm). The Young–Laplace equation can be used to estimate the pressure jump across the interface of the embryo bubble, $\Delta p = \beta / R_b = 0.76$ MPa taking into account the pseudo 2D geometry and using the value of β from Table 2. Via the Clausius–Clapeyron equation, the value of the pressure jump can be converted into the necessary liquid superheat to sustain the existence of the bubble, $\Delta T = \Delta p T_{sat} / (\rho_v h_{lv}) = 6.88$ K using the fluid properties in Table 2. Therefore, nucleation is expected to occur when the fluid region near the wall reaches an activation temperature of about 115 K, or 0.96 in MD units. Nucleation happens in the MD system when $t \approx 4000$. Fig. 5b, discussed later in the text, will show that the near-wall ($y = 0$) liquid temperature at $t = 4312$, shortly after nucleation, is 0.95, which is in agreement with our estimation above. Note that the time required for nucleation is similar to the value reported by Lavino et al. [19] for nucleation in a Lennard-Jones system under analogous conditions ($t = 4000 - 5000$), using the MD simulation software LAMMPS. The bubble nucleates inside the cavity in agreement with previous studies for hydrophilic walls, and quickly grows emerging from the cavity and expanding in all available directions, see Fig. 3b. As time elapses and more heat is introduced into the system, the bubble grows due to liquid evaporation at the interface. It will be shown in Section 4.2.3 that the liquid–vapour phase-change mechanism is well described by the

Hertz–Knudsen–Schrage equation, which was obtained by modelling the motion of the fluid molecules near the interface using the kinetic theory of gas [1]. Owing to the hydrophilic walls, the bubble retains a spherical shape while it grows outside the cavity. A thin layer of liquid remains trapped beneath the bubble over the horizontal surface. This thin liquid film does not evaporate despite the high local temperatures, due to the attraction exerted by the solid wall, and thus is often referred to as a non-evaporating adsorbed film [60]. As the bubble expands, the free liquid–vapour surface at the top of the domain moves upwards and the pressure in the vapour layer on top of it increases slightly. This layer of vapour is therefore necessary to avoid an excessive increase in pressure that would occur if only liquid were initially present inside the computational domain. During the bubble growth, the liquid is pushed radially towards the external domain boundaries and the temperature field is advected accordingly; as a result, two symmetric regions with increased liquid temperature values form at the sides of the bubble, next to the wall (Fig. 3f). The liquid in close contact with the hot wall exhibits slightly lower density than that far from the wall, although this is not sufficient to trigger any new nucleation event outside the cavity. The bubble grows in the vertical direction faster than temperature diffusion within the liquid phase (compare Figs. 3e and 3f), and thus the average temperature around the vapour–liquid interface decreases over time. Inside the bubble, the mean temperature value is always below that of the surrounding liquid.

The bubble volume and radius over time are shown in Fig. 4a. The bubble volume in the MD is calculated at each time instant by fitting a mesh over the MD domain and computing the sum of the cell volumes where $\rho < (\rho_l + \rho_v)/2 \approx 0.34$ (or where $\rho < \rho_l/2$, since $\rho_v \ll 1$). The bubble radius reported in Fig. 4a corresponds to the radius of the circular arc fitting the liquid–vapour interface when the bubble grows outside the cavity, identified as explained in Fig. 4d. The bubble radius follows a linear trend over time for $t \leq 6000$, in agreement with Rayleigh solution for the inertia-controlled growth stage of the bubble [1]. The slope of the curve identifies the bubble growth rate dR/dt and corresponds to 0.02 in reduced MD units, or 3.16 m/s in SI units. The bubble growth subsides slightly for $t > 6000$, which may be due to the fact that the bubble is expanding in a region of fluid which is farther from the hot wall. At the end of the simulation, $t = 6800$, the bubble has reached a final volume of $V_v = 2.4 \cdot 10^5$ ($9.43 \cdot 10^3$ nm^3) and a radius of about 100σ (34 nm).
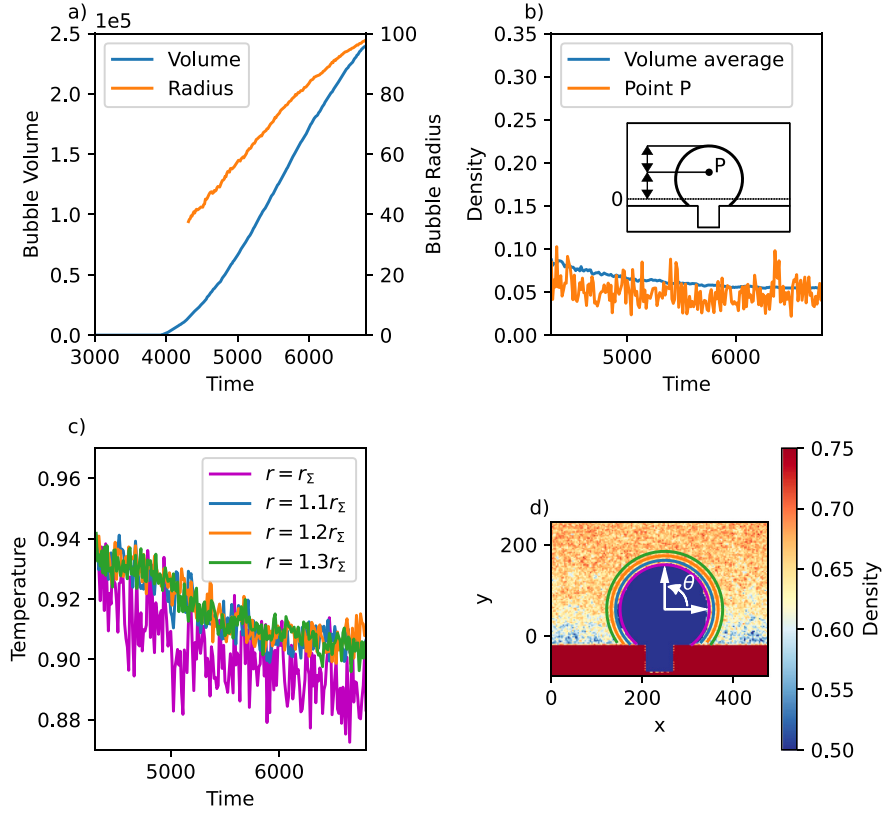
Fig. 4. Analysis of the growing vapour bubble and surrounding liquid region from the MD-only simulation. (a) Plot of the temporal evolution of the bubble volume and radius of the fitted circle, calculated as illustrated in (d). The system reaches a favourable state for nucleation at $t \approx 4000$, where the bubble starts to grow. (b) Density of the vapour phase within the bubble over time, calculated as a spatial average within the bubble (blue curve) and as a local value at point P; P is located halfway between the $y = 0$ boundary and the bubble cap and remains within the bulk vapour bubble region as the bubble grows. (c) Circumferential average, calculated over the top half of a circular arc ($0 < \theta < \pi$), of the temperature at the bubble interface ($r = r_\Sigma$) and near the interface at increasing distance from it. A schematic of the arcs used to calculate the spatial averages in (c) is shown in (d). The interfacial arc ($r = r_\Sigma$) is obtained by first flagging the interfacial cells (in the 2D xy plane at $z = L_z/2$) where a jump $|\Delta\rho| > 0.3$ occurs between adjacent cells in any of the spatial directions. Subsequently, a circular arc is computed by a least squares fitting to the interfacial cell centres located above the solid wall ($y > -20\sigma$).

In the MD data, the bubble region is identified by a sudden drop in density that occurs when liquid is converted into vapour. A volume average density for vapour within the bubble is obtained by averaging ρ in the cells marked as vapour, i.e. where $\rho < 0.34$. The value of this average density within the bubble is plotted against time in Fig. 4b, along with the time evolution of density recorded at a point P inside the bubble. The location of P is computed as the point along the centre line of the domain ($x = L_x/2$) that is equidistant from the top of the bubble and the axis $y = 0$. The reason for calculating the vapour density in P is to extract a representative value for the vapour density within the bubble to be used in the CFD simulation. The average vapour density reaches a steady regime after a quick transient that occurs right after nucleation and approaches a value of approximately $\rho \approx 0.05$. The density recorded at the (time-evolving) location of point P exhibits small amplitude fluctuations and a mean value slightly below the corresponding volume-average one. Such a difference is due to the fact that the liquid–vapour interface in MD is not sharp, but is a region of finite thickness where density varies in a continuous manner from the bulk liquid to the bulk vapour value [1]. Shortly after nucleation, when the bubble is still small, the interface thickness is large relative to the bubble size and thus the average vapour density value is significantly influenced by the denser vapour region on the vapour side of the interface. As the bubble grows, the interface thickness remains constant and thus the average vapour density within the bubble reduces and converges asymptotically to the bulk value measured in P. Note that the

local value of the vapour density in P remains approximately constant over time as the bubble continues growing. Accordingly, the value of the vapour density in the CFD model is set to $\rho_v^{CFD} = 0.05$.

An important output from the MD simulation is the temperature field in the interface region. An accurate prediction of the temperature profiles around the interface is a crucial requirement for the coupled MD-CFD framework in order to reproduce the same bubble growth rate as shown in the MD results, because the phase-change rate in the CFD model is driven by the temperature difference ($T - T_{\mathrm{sat}}$) at the interface (see Eq. (12)). To this end, the circumferentially-averaged profiles of temperature around the vapour–liquid interface in the MD simulations are plotted in Fig. 4c at four different distances from the centre of the bubble. The first profile ($r = r_\Sigma$) is a plot along the top-half of a circular arc (i.e., $0 < \theta < \pi$ in the schematic in Fig. 4d) fitted to the vapour–liquid interface, whilst $r = 1.1r_\Sigma, 1.2r_\Sigma, 1.3r_\Sigma$ are plots at incremental distances ($10, 20, 30\%$ of the bubble radius, respectively) from the centre of the bubble. A representation of the circular arcs, along with the local reference system, is shown in Fig. 4d. The profile of temperature at $r = r_\Sigma$ exhibits strong fluctuations over time, whilst the other three plots are characterised by smaller amplitudes and larger mean temperatures than those detected at the interface. The latter is expected as evaporation of liquid at the interface cools down the fluid locally. As time elapses and the bubble grows, the liquid temperature around the interface decreases due to the dissipation of latent heat induced by evaporation and by the fact that the bubble expands into
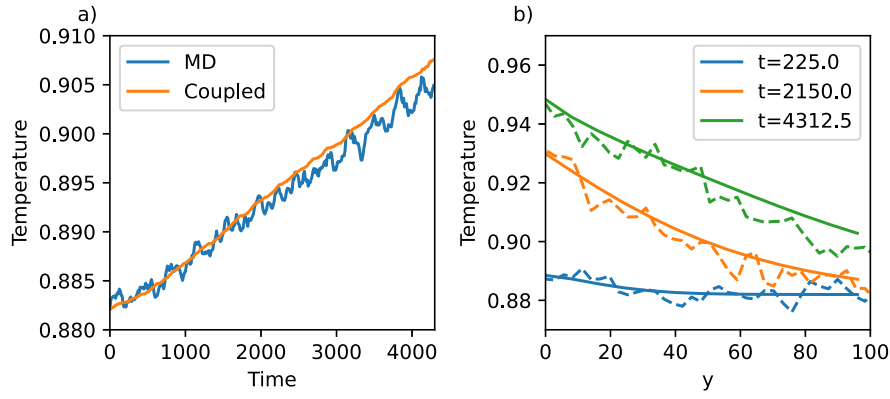
Fig. 5. Analysis of temperature diffusion into the liquid system prior to bubble nucleation. (a) Temporal evolution of the average liquid temperature in a sub-domain of width L_x and height 200σ ($0 \leq y \leq 200\sigma$). (b) Plot of vertical temperature profiles, averaged across x and z, for three different time instants; dashed and solid lines refer to Molecular Dynamics and coupled simulations, respectively.

a region of lower temperature, as the interface moves away from the heated wall.

4.2. Coupled MD-CFD simulation

4.2.1. Verification of thermal coupling

A first verification test for the consistency of the coupling between MD and CFD fields is a comparison of the temperature fields achieved in the coupled framework with that of the MD-only simulation. If the coupling is correct and the thermophysical properties of the fluid in the two systems coincide, the temperature profiles in the MD-only and coupled cases should match as time elapses, which is eventually an important requirement to achieve the same bubble growth rates. Fig. 5 presents temporal and spatial evolution of the liquid temperatures prior to bubble nucleation.

The evolution of the volume-average temperature over time in a sub-domain of width L_x and height 200σ ($0 \leq y \leq 200\sigma$) for MD-only and coupled simulations is displayed in Fig. 5a. The temperature of the liquid in the CFD is initially set to $T = 0.882$ to match the MD data in the liquid, and it grows as a linear function of time as more heat is released by the solid wall. Note that at this stage only liquid exists in this region, since nucleation occurs at $t \approx 4000$. The volume-average temperatures obtained with MD and coupled frameworks agree fairly well, with a slight tendency of the MD-CFD model to overestimate temperature as time elapses. It is plausible that the thermal diffusivity value set in the coupled model does not match exactly that of the Lennard-Jones fluid in the MD simulation. It was verified that a best match with the MD temperature plot in Fig. 5a would be recovered by setting a thermal diffusivity about 15% lower, which is consistent with the values reported in the literature [38]. Fig. 5b shows temperature profiles along the vertical coordinate y at different time instants. The profiles are averaged in space across the x and z coordinates. Note that the reference $y = 0$ coincides with the MD-CFD coupled boundary, which is located 20σ above the top surface of the solid wall. The temperature profiles over time emphasise the development of the thermal boundary layer upon the heated wall as time elapses, which is captured in both the MD and coupled solutions. While the temperature profiles calculated from the CFD results appear smooth, the molecular solution exhibits spatial fluctuations as typical in MD. Nonetheless, the temperature profiles obtained with the coupled solver fit well the MD data. As observed in Fig. 5a, there is a slight trend for the coupled solver to overestimate temperature farther from the heated wall at later stages, which can be ascribed to a minor mismatch of the liquid properties responsible for thermal transport. Overall, the good agreement of MD and hybrid solver temperature profiles indicates

that the temporal evolution of the thermal energy generated in the MD domain is correctly communicated to the CFD solution. However, for a seamless match of MD and CFD temperatures evolution over time, it may be preferable to tune accordingly the liquid thermal conductivity in the continuum model.

4.2.2. Verification of mass conservation

The second test for coupling consistency is mass conservation, and is performed by verifying that the mass of vapour received by the CFD solution through the coupled boundary matches that sent by the MD. To facilitate the test, phase-change is disabled in the CFD model, so that the mass of vapour in the CFD domain can only come from the MD input through the coupled boundary. The mass of vapour contained in the CFD domain at a given time instant can be calculated via a volume integral of the VOF phase fraction:

$$M_v^{CFD}(t) = \rho_v^{CFD} \int_{V_{CFD}} (1 - \alpha) \, dV \tag{14}$$

Owing to the boundary conditions set to the CFD domain, any variation of M_v^{CFD} over time can be attributed only to the inflow from the coupled boundary. The mass of vapour introduced into the CFD domain through the coupled boundary ($y = 0$) by the MD can be calculated as an integral along the coupled boundary:

$$M_{v,y=0}^{MD}(t) = \int_0^t \int_{S_y} \rho_v^{MD} v \, dS \, dt \tag{15}$$

where ρ_v^{MD} and v are the density of vapour and the y–component of the velocity field, respectively, and dS is the infinitesimal surface area with surface integral over S_y, which denotes the $x - z$ surface at $y = 0$. In the MD, the density of vapour ρ_v^{MD} for use in Eq. (15) is highly susceptible to fluctuations. The density of the fluid ρ^{MD} is more reliable in each MD control volume, using the averaging process outlined in Section 2.1. Hence, a criterion is necessary in order to define whether a MD control volume contains vapour or liquid and, in the case of vapour, obtain its density in the bin. The density half way between vapour and liquid can be assumed to be a threshold $\rho_c = 0.5(\rho_l^{CFD} + \rho_v^{CFD})$. Two different expressions to calculate ρ_v^{MD} in Eq. (15) were tested:

$$\rho_v^{MD,1} = \begin{cases} \rho^{MD}, & \text{if } \rho^{MD} \leq \rho_c \\ 0, & \text{if } \rho^{MD} > \rho_c \end{cases} \tag{16}$$

where, if the MD bin is identified as a vapour bin (MD density below the average of liquid and vapour specific CFD densities), the density used in Eq. (15) is set identical to the MD density in the bin, which may vary both in space and time. The second expression is:

$$\rho_v^{MD,2} = \begin{cases} \rho_v^{CFD}, & \text{if } \rho^{MD} \leq \rho_c \\ 0, & \text{if } \rho^{MD} > \rho_c \end{cases} \tag{17}$$

where, if the MD bin is identified as a vapour bin, the density in Eq. (15) is set equal to the vapour density in the CFD model, which is a constant.

A comparison of the mass of vapour calculated from the coupled framework using Eq. (14) and from the MD mass flux at the coupled boundary using Eq. (15), with either Eq. (16) or (17), is displayed in Fig. 6a. The vapour mass in the CFD domain increases as time elapses, as expected, in qualitative agreement with both $MD, 1$ and $MD, 2$ curves. The vapour mass in the CFD remains slightly below the curve for $MD, 1$ at intermediate stages ($4000 < t < 6000$). This is due to the fact that in Eq. (16) the vapour mass flow rate through the coupled boundary for MD is evaluated using the actual MD density, ρ^{MD}, which is in general slightly higher than the value of $\rho_v = 0.05$ measured at the centre of the bubble (see Fig. 4b) and set in the CFD model. When Eq. (17) is utilised to calculate the vapour density in the MD, the resulting curve $MD, 2$ in Fig. 6a matches exactly the bubble volume over time in the CFD. This is due to the fact that the vapour density in the CFD model is constant, and thus the same value must be used when verifying the balance from the MD side. Since Eq. (13) is used to calculate the VOF phase fraction from the MD density data, the CFD model receives either pure liquid ($\alpha = 1$, with $\rho \equiv \rho_l^{CFD}$) or pure vapour ($\alpha = 0$, with $\rho \equiv \rho_v^{CFD}$). It is therefore necessary, to assess the consistency of the density coupling, to use the CFD value of the vapour density in Eq. (15). Although the slight deviation between curves $MD, 1$ and $MD, 2$ in Fig. 6a may suggest that a CFD model with variable vapour density would be necessary to recover an exact match between MD and CFD vapour flow rates at the coupled boundary at every time instant, the exact match between the CFD data and the $MD, 2$ curve emphasises that the MD-CFD coupling algorithm ensures a consistent exchange of density data.

To perform the density coupling test discussed above, phase-change was disabled in the CFD model. Figs. 6b and 6c present a comparison of the contours of density and temperature obtained in the MD-only and coupled simulations. As expected, the size of the bubble as predicted by the continuum model is smaller compared to the corresponding atomistic simulation. The difference is due to the lack of phase-change in CFD and, therefore, the change in bubble volume induced by evaporation is completely missed. It will be shown in the next section that a good match of bubble volume between MD and coupled simulation can be achieved once the phase-change model is activated. Nonetheless, the left hand side of Fig. 6b demonstrates that the liquid–vapour interface transitions smoothly from the MD region ($y \leq 0$) to the CFD region ($y \geq 0$) and the interface orientation at the coupled boundary is well preserved by the coupling architecture. The contours of temperature show a qualitative agreement between the two numerical approaches, with a lower temperature distribution inside the bubble and a thermal boundary layer that grows near the wall. Such boundary layer is thicker near the left and right boundaries of the domain (i.e., $x = 0$ and $x = L_x$, respectively), due to the velocity field induced by the expansion of the bubble.

4.2.3. Boiling dynamics and parametric analyses

In this section, the results of the coupled model with phase-change activated are presented. The phase-change model in the CFD solver requires knowledge of the saturation temperature and of the accommodation coefficient, see Eq. (12), which are not readily available from the MD data. Fig. 4c indicates that the average liquid temperature near the interface in the MD simulation decreases from 0.94 to about 0.9 as time elapses. Thus, it is expected that the saturation temperature of the fluid has values within this range, which is chosen for the parametric analysis conducted below. As a first guess value, $T_{sat} = 0.9$ is adopted, as this is the fluid temperature at which liquid and the vapour layer above it coexist at the end of the equilibration stage in the MD. The values of the accommodation coefficient are debated even for an ubiquitous fluid such as water, for which values spanning three orders of magnitude were reported [18,61]. Ishiyama et al. [58] employed MD simulations of evaporation and condensation of a planar

interface to calculate the values of the accommodation coefficient of Argon, for temperatures in the range $70 - 130\,K$, corresponding to 0.58–1.08 in reduced units. The accommodation coefficient was observed to decrease from $\gamma \approx 1$ at $70\,K$ to $\gamma = 0.44$ at $130\,K$. A similar setup was applied by Liang et al. [34] to measure accommodation coefficients for Argon undergoing phase-change across a planar interface, reporting similar values. Accommodation coefficients quickly dropping from $\gamma = 0.8$ at $T = 100\,K$ to $\gamma < 0.1$ for $T \geq 120\,K$ were reported by Matsumoto [62]. It is difficult to calculate the accommodation coefficient from the present MD simulations owing to the curved and non-stationary dynamics of liquid–vapour interface of the bubble, however, the range of values reported in the literature may serve as a benchmark. Hence, a series of simulations with the coupled MD-CFD model was performed by parametrically varying T_{sat} and γ within the range $T_{sat} = 0.9 - 0.95$ and $\gamma = 0.1 - 1$.

A first set of simulations was run by disabling condensation in the CFD model, thus only allowing for evaporation. This was achieved by setting to zero the minimum value possible for the interphase mass transfer in Eq. (12). Figs. 7 and 8 present a comparison of the results obtained with the MD and coupled MD-CFD model, for three selected pairs of saturation temperatures and accommodation coefficients. Fig. 7a compares the global amount of vapour mass in the CFD domain with that measured for the bubble in the region of the MD domain coinciding with the CFD domain ($y > 0$). The vapour mass in the CFD domain is calculated using Eq. (14); the corresponding vapour mass within the bubble in the MD domain is calculated using:

$$M_{v,y>0}^{MD}(t) = \int_V \rho_v^{MD}\,dV \tag{18}$$

where the volume V corresponds to the MD volume above $y = 0$ but below the vapour layer on top of the domain, so that only the mass of vapour corresponding to the bubble is included in the calculation. The vapour density in the MD is calculated using Eq. (17). For $T_{sat} = 0.9$, an accommodation coefficient of $\gamma = 0.2$ is found to yield the best agreement with the MD bubble volume data and thus this is the case selected for display in Figs. 7 and 8; the full results of the parametric analysis will be discussed later in this section. A video showing a side-by-side comparison of MD-only and hybrid MD-CFD bubble growth and corresponding density fields is provided as a Supplementary Content file. Ishiyama et al. [58] calculated a value of the accommodation coefficient of $\gamma \approx 0.7$ for a Lennard-Jones fluid at $T = 0.92$, whereas Matsumoto [62] computed $\gamma = 0.4$ for Argon at the same temperature. Although the MD simulations of Ishiyama et al. [58] and Matsumoto [62] were performed for a planar interface, it is possible that a value of $\gamma = 0.2$ to describe interphase mass transfer when $T = 0.9$ is an underestimation. As a matter of fact, the value $T_{sat} = 0.9$ was chosen upon the MD results for a flat liquid–vapour interface at equilibrium, whereas the value of saturation temperature representative of the interphase mass transfer across the bubble may be slightly higher, owing to the interface curvature and Laplace jump in pressure. Hence, two additional simulations were run by slightly increasing the saturation temperature to $T_{sat} = 0.91$ and 0.92, while setting $\gamma = 0.7$ in agreement with Ishiyama et al. [58]; the results are included in Fig. 7 alongside those for $T_{sat} = 0.9$ and $\gamma = 0.2$. Upon an increase in saturation temperature, the evaporation rate decreases but the increase in the accommodation coefficient partially counteracts this effect. The coupled simulation results in terms of bubble mass over time in Fig. 7a for $T_{sat} = 0.91$ and $\gamma = 0.7$ are slightly above the MD data, whereas those for $T_{sat} = 0.92$ and $\gamma = 0.7$ remain slightly below. Thus, with a value of the saturation temperature between $T_{sat} = 0.91$ and 0.92 and an accommodation coefficient of $\gamma = 0.7$, consistent with literature data, it is possible for the coupled simulation to achieve the same bubble growth as in the MD. Note that all CFD curves exhibit faster bubble growth during the initial stages. This can be ascribed to the effect of the bubble interface curvature, which has been observed to increase the surface tension of nanobubbles of radius smaller than
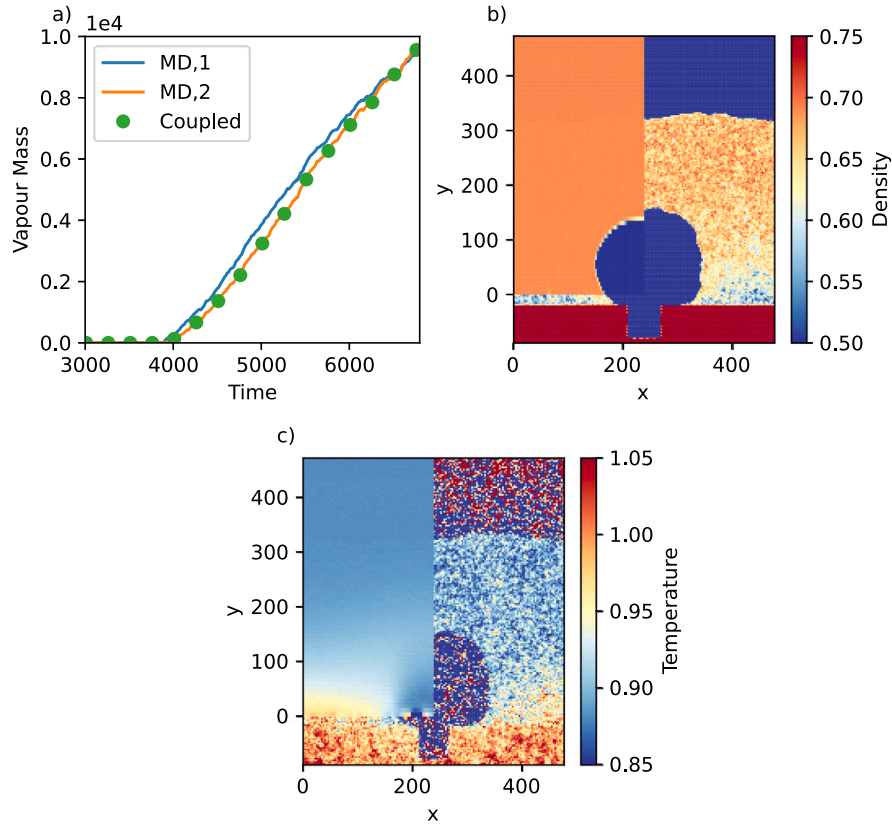
Fig. 6. Comparison between Molecular Dynamics and coupled simulation framework with phase-change disabled in the CFD model. (a) Plot of vapour mass in the CFD domain for the coupled simulation over time (Eq. (14)), compared with the vapour mass inflow through the coupled boundary sent by the MD (Eq. (15)); Eq. (16) is used to calculate ρ_v^{MD} in the curve named $MD,1$ while Eq. (17) is used for $MD,2$. (b,c) Contours of (b) density and (c) temperature near the end of the simulation, $t = 6800$. In each plot, the right half shows the MD solution, whilst the left half represents the field contours from the coupled framework. Due to the absence of phase-change in the continuum model, the size of the bubble is smaller compared to the MD simulation.

20σ [63]. It is thus possible that the actual saturation temperature in the MD, shortly after the formation of the bubble embryo, is higher than the constant value set in the CFD. This is manifested by a more gradual increase of the bubble growth rate over time in the MD solution compared to the hybrid simulation. Fig. 7b shows the temporal evolution of the circumferentially-averaged temperature profiles around the bubble interface, for four different radial distances from the centre of the bubble. Only the top half of the bubble ($0 < \theta < \pi$) is used for the calculation of the average temperatures, see Fig. 4d for the definition of the circular arcs. The centres and radii of the four arcs are chosen based on the MD results, and thus the same circles are utilised to extract both MD and CFD data, independently of the bubble size in the CFD solution. The average temperature decreases over time due to the combined effect of dissipation of latent heat during the vaporisation process and movement of the interface towards a colder liquid region. The decreasing temperature trend in the MD is correctly reproduced by the coupled simulations. An excellent match is observed for temperatures extracted at the interface, $r = r_\Sigma$, during the earlier stages of bubble growth ($t < 6000$), whereas the coupled simulation tends to slightly overestimate the MD temperatures at later time. This may be due to the fact that the saturation temperature is not constant in reality, but it decreases as the bubble grows and the pressure within the bubble decreases. It is also worth mentioning that temperatures for $r = r_\Sigma$ are averaged over a circle fitting the bubble interface and, since the bubble in the MD is not exactly circular at later stages, part of the circle is within the bubble where temperatures are lower. When regions farther from the interface are considered, $r > r_\Sigma$, the coupled simulation slightly underpredicts temperatures at

earlier stages of bubble growth whereas a very good match with MD is achieved as $t > 5000$. The reason of the underprediction at early stages is due to the slightly higher bubble growth rate achieved in the CFD simulations shortly after nucleation. The locations and radii of the circles where temperature is extracted for both CFD and MD are chosen based on the bubble profile in the MD solution. With the bubble in the CFD being slightly larger than the MD, the radial coordinates $1.1r_\Sigma$, $1.2r_\Sigma$ and $1.3r_\Sigma$ are closer to the liquid–vapour interface in the CFD and thus temperatures are lower. This mismatch vanishes as time elapses and the agreement between MD and CFD bubble sizes improves. Overall, the good agreement of MD and CFD bubble growth rates and near-interface temperature fields provides confidence that the use of the Hertz-Knudsen-Schrage equation to estimate the interphase mass transfer in the CFD model is appropriate to describe the phase-change process at the molecular scale.

The comparison of the coupled simulations with evaporation-only phase-change and MD results is concluded with the contours of density and temperature reported in Fig. 8a,c for $T_{sat} = 0.91$ and in Fig. 8b,d for $T_{sat} = 0.9$, respectively. The two CFD simulations provide almost identical solutions and a significantly better agreement against MD-only results is achieved compared to the case without phase-change (Fig. 6b,c). This is particularly evident in Fig. 8a and 8b, where the bubble caps in the coupled cases reach the same vertical coordinate as the MD solution. The bubble shape in the MD is less regular than that in the CFD framework, which appears more circular, due to the intrinsic velocity fluctuations in the MD. These are also responsible for the nonuniform temperature field within the bubble.

Systematic analyses of the effects of saturation temperature, accommodation coefficient and condensation on the bubble growth are
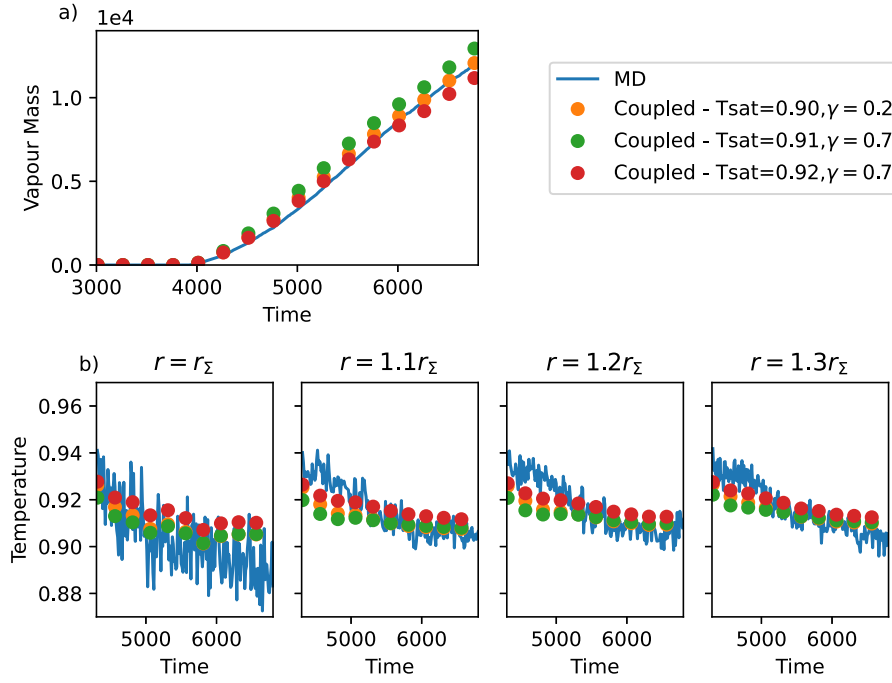
Fig. 7. Comparison between Molecular Dynamics and coupled simulation framework; phase-change (evaporation only) is enabled in the CFD model. (a) Plot of the vapour mass within the bubble for $y > 0$ versus time. The MD curve is computed from the volume integral of the density field, see Eq. (18). (b) Temporal evolution of the circumferentially-averaged ($0 < \theta < \pi$) temperatures at the bubble interface ($r = r_\Sigma$) and near the interface at increasing distance from it; see Fig. 4d for a sketch of the circular arcs used to calculate temperatures. The centres and radii of the arcs are based on the MD bubble data, and the same arcs are used to extract temperatures for both CFD and MD solutions.
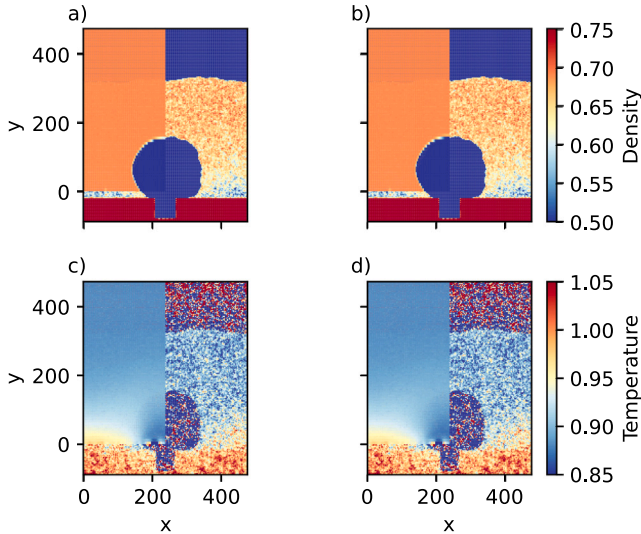

Fig. 8. Comparison between Molecular Dynamics and coupled frameworks for density (a,b) and temperature (c,d) fields; phase-change (evaporation only) is enabled in the CFD model. (a, c) $T_{sat} = 0.91$, $\gamma = 0.7$. (b, d) $T_{sat} = 0.9$, $\gamma = 0.2$. The right half of each figure shows the MD solution, whilst the left-half represents the coupled model. The snapshots are taken at $t = 6800$. A better agreement against MD is observed, compared to the case without phase-change (see Fig. 6b) in terms of size and shape of the bubble. A video showing the temporal evolution of the hybrid and MD-only density fields as displayed in panel (b) above, for $T_{sat} = 0.9$ and $\gamma = 0.2$, is provided as supplementary content.

provided with Fig. 9. Fig. 9a depicts the mass of vapour contained in the bubble over time, for $\gamma = 1$ and saturation temperature varying within the range $T_{sat} = 0.9-0.95$; only evaporation is enabled in the CFD phase-change model. Increasing the saturation temperature reduces

the mass transfer at the interface and, therefore, the growth rate of the bubble decreases accordingly. The highest saturation temperature tested, $T_{sat} = 0.95$, does not lead to a sufficient evaporation rate for the bubble to grow in agreement with the MD growth rates, resulting in an underestimation of the bubble volume even when using $\gamma = 1$. The growth rate obtained with $T_{sat} = 0.92$ is the closest to the MD data that can be achieved when setting $\gamma = 1$. However, a value of $\gamma = 1$ is significantly higher than that reported in the literature for the evaporation of a Lennard-Jones fluid at this temperature [58], and thus the good agreement with the MD data in Fig. 9a may simply be due to $T_{sat} = 0.92$ being an overestimation of the saturation temperature in the MD. Another set of simulations was run by reducing the saturation temperature to $T_{sat} = 0.9$ and varying γ in the range $\gamma = 0.1 - 1$ to investigate the effect of γ on the bubble growth. The results are reported in Fig. 9b and indicate that $\gamma = 0.2$ yields the best agreement with the MD data, as previously discussed. The range of variation of the bubble mass at the end of the simulation is narrower than the range of variation of γ, with M_v^{CFD} for $\gamma = 1$ being about 50% higher than the value achieved for $\gamma = 0.1$. Note that decreasing the accommodation coefficient has the effect of increasing the temperature near the interface, due to the accumulation of sensible heat while the latent heat dissipated by the evaporation process is reduced. Finally, Fig. 9c displays the results obtained by enabling both evaporation and condensation in the CFD model, for the same values of T_{sat} and γ used to produce the curves in Fig. 9b. Condensation occurs on the bubble cap at the later stages, when the bubble has grown sufficiently large to emerge from the superheated thermal boundary layer developing over the heated wall. No appreciable differences can be observed in the growth rates of Fig. 9c and 9b for $\gamma \leq 0.4$. This is due to the fact that the bubble size is smaller due to the low accommodation coefficient and thus a larger portion of it remains in the superheated liquid zone, but also because the small accommodation coefficient reduces the impact of the vapour-to-liquid condensation mass transfer. For $\gamma > 0.4$, the impact of condensation is more apparent and is manifested by a subside of the bubble growth rate at later time instants, where condensation
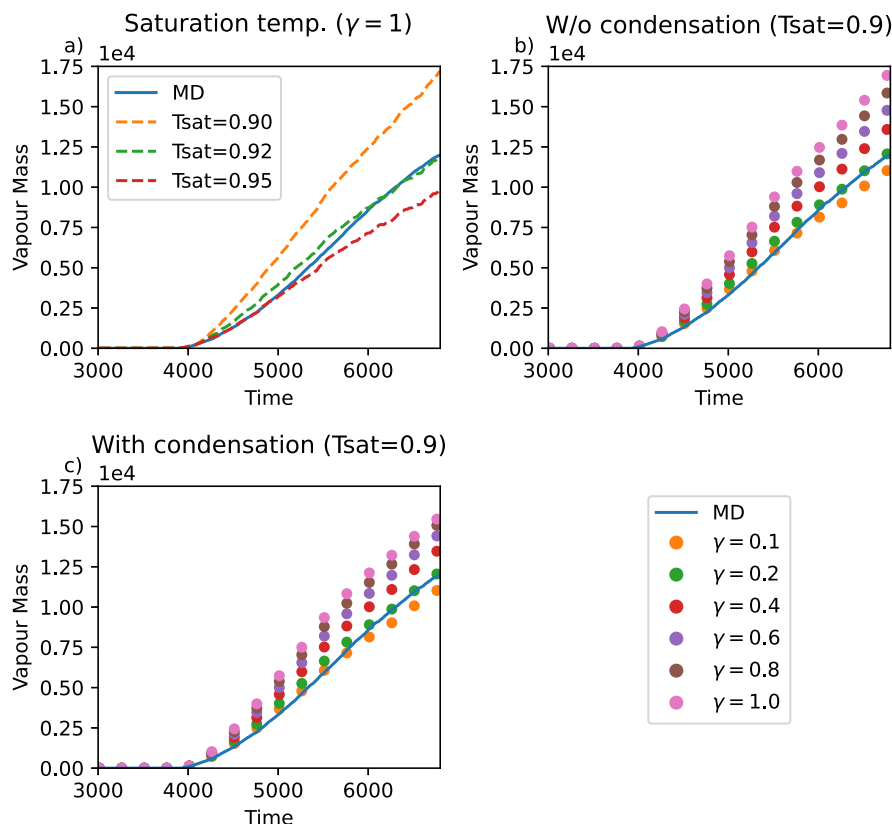
Fig. 9. Systematic analysis of the effect of T_{sat} and γ on the coupled framework. The three figures provide plots of the vapour mass within the bubble for $y > 0$ versus time. (a) Coupled model with phase-change accounting only for evaporation, with $\gamma = 1$ and $T_{sat} = 0.9 - 0.95$. (b) Coupled model with phase-change accounting only for evaporation, with $T_{sat} = 0.9$ and $\gamma = 0.1 - 1$. (c) Coupled model with phase-change accounting for both evaporation and condensation, with $T_{sat} = 0.9$ and $\gamma = 0.1 - 1$.

of vapour on the top of the bubble occurs due to the subcooled fluid. For $\gamma = 1$ and $T_{sat} = 0.9$, the bubble volume measured at $t = 6800$ in the presence of both condensation and evaporation is about 15% lower than that achieved by the simulation run disregarding condensation. The best match between the MD solution and that of the coupled MD-CFD framework with $T_{sat} = 0.9$ remains the one obtained with $\gamma = 0.2$ even when the CFD phase-change model accounts for the complete mass transfer process including both evaporation and condensation.

5. Discussion: Perspectives for multiscale simulations

The results presented in the previous section demonstrate that it is possible, for a heat and mass transfer model based on the solution of the continuum Navier–Stokes equations, to reproduce the dynamics of a bubble shortly after nucleation in good agreement with those obtained using a molecular description. This paves the way for multiscale simulations where MD handles only the near-wall region to capture nucleation and contact lines, whereas the CFD extends the applicability of the simulation towards much larger scales. Still, with the present coupled framework the spatial and temporal scales are dictated by the process at the molecular scale, and thus appropriate decoupling of scales is necessary to bring the modelling framework towards engineering scales, e.g. to achieve millimetre-sized bubbles.

Spatial decoupling can, in part, be easily achieved by using an adaptive mesh in the CFD model. Nonetheless, since MD requires substantial computational efforts to achieve a domain size necessary to accommodate the growing bubble, a two-way domain decomposition coupling of MD and CFD becomes essential to limit the MD extension to only a few nanometres above the heated wall [33]. As the bubble

grows, eventually the contact line will approach the boundaries of the MD domain. A potential way forward to continue following the contact line motion using MD and domain decomposition coupling, is to activate on-the-fly new MD runs exclusively dedicated to modelling the contact line, as done for example by Wu et al. [31] in the context of droplet spreading over a solid surface.

The intermittent temporal coupling strategy presently adopted is suitable to capture the early stages of bubble growth. The capillary time-step constraint [55] requires the CFD time-step to scale with $\Delta t^{CFD} \sim \Delta^{3/2}$, with Δ being the CFD mesh size, and for $\Delta \approx 1\,\mathrm{nm}$ this becomes comparable to the time interval necessary for averaging MD data thus enabling synchronous temporal coupling. Municchi et al. [45] performed CFD simulations of nucleate boiling with a very fine mesh of $\Delta = 0.5\,\mu\mathrm{m}$ to capture the evaporation microlayer beneath the growing bubble, and the time-step during the initial growth stage was on the order of $10^{-10}\,\mathrm{s}$. This suggests that synchronous coupling may still be acceptable during the first few nanoseconds of a CFD simulation of boiling, with the bubble being only few micrometres in size. However, time-scale decoupling becomes necessary to follow the growth of the bubble when the separation of scales between molecular and continuum mechanics becomes intractable, e.g. steam bubbles in pool boiling at atmospheric pressure detach from a hot surface due to buoyancy when they reach an equivalent diameter of 3–4 mm, which takes about $10\,\mathrm{ms}$ from the instant of nucleation (or, better, from the instant at which the bubble becomes visible) [8]. Specifically, the CFD and MD models must evolve asynchronously to reduce the number of MD time-steps required to achieve scales of micro-/milliseconds. A number of techniques have been devised in the literature, for example Lockerby et al. [54] proposed an asynchronous intermittent coupling strategy where the micro and macro models evolve along different time-scales

and the frequency of data exchange depends on a dimensionless scale-separation number. The time-burst scheme is another popular method to decouple time-scales in unsteady simulations with domain decomposition [21]. With this technique, the MD simulation is performed over a time interval which is much smaller than the CFD time-step, and results are then extrapolated to the time instant at which the next CFD time-step begins.

A different coupling strategy that can be exploited to incorporate molecular-level information into a CFD model of boiling at reduced computational cost is heterogeneous coupling [64], where MD and CFD simulations are performed separately. Since the present coupled simulations revealed that the bubble in the CFD model evolves consistently with the MD description, a series of MD simulations in a small domain (e.g., a box of 10 nm) can be run beforehand for different wall temperatures to determine whether nucleation occurs or not. The output data could be stored in a library and used in the CFD simulation as a nucleation activation model, replacing state-of-art methods where the activation temperature is prescribed [16,17]. The contact line dynamics in the CFD model, e.g. advancing, receding contact angles, Navier slip, can be extracted from the same series of MD simulations and implemented via intermediate models such as Molecular Kinetic Theory or Tanner's law [22,65].

6. Conclusions

This article presented a hybrid atomistic–continuum framework for coupled simulations of nucleate boiling. A domain decomposition coupling method was utilised, where the near-wall region is solved by a Molecular Dynamics description and the bulk flow region is solved by a continuum description based on the Navier–Stokes equations. The latter features a multiphase CFD model based on the Volume Of Fluid method and the Hertz-Knudsen-Schrage equation to calculate the interphase mass transfer induced by evaporation and condensation at the liquid–vapour interface. A one-way coupling was realised, where the MD density, velocity and temperature data are used to set time-dependent boundary conditions for the CFD over a coupled boundary. This coupling strategy allows for molecular-level physics such as bubble nucleation and contact line dynamics to be handled by MD, without the need for closure models in the CFD. The modelling framework was demonstrated by means of a MD-CFD coupled simulation of boiling of a Lennard-Jones fluid over a heated wall with a geometrical imperfection acting as a nucleation spot. The results obtained with the coupled framework in terms of time-dependent bubble volume, phase-change rates, bubble dynamics and evolution of the temperature field agree quantitatively well with those achieved by a MD-only simulation. The coupled framework is capable of reproducing the bubble growth rate over time from nucleation until a bubble size of about 70 nm, demonstrating the accuracy and robustness of the coupling architecture. This also shows that the continuum fluid dynamics description based on the Navier–Stokes and energy equations is capable of correctly capturing the main heat and mass transfer mechanisms responsible for bubble growth at the nanoscale. The good agreement of the bubble size and of the fluid temperature in the proximity of the liquid–vapour interface throughout the duration of the simulation suggests that the Hertz-Knudsen-Schrage equation is sufficiently accurate to model evaporation and condensation phase-change at the nanoscale. The comparison between CFD and MD is also useful to inform values of the accommodation coefficient, which is often treated as an empirical parameter in continuum-scale phase-change models. The values obtained in this work show good agreement to the literature for phase-change in a Lennard-Jones fluid.

The present coupled MD-CFD framework paves the way towards multiscale simulations of boiling, that can be achieved either by the proposed domain decomposition coupling augmented with opportune strategies to decouple temporal and spatial scales, or by a computationally cheaper heterogeneous coupling method where targeted MD simulations can be leveraged to set closure parameters in CFD models.

The numerical framework developed in this work, together with installation, user and tutorial guides, also including the setup files utilised to perform the simulations whose results are presented in this article, are publicly available on Github (github.com/Crompulence/CPL_APP_OPENFOAM).

CRediT authorship contribution statement

Gabriele Gennari: Writing – original draft, Visualization, Validation, Methodology, Investigation. **Edward R. Smith:** Writing – review & editing, Supervision, Software, Resources, Methodology, Conceptualization. **Gavin J. Pringle:** Writing – review & editing, Software, Methodology. **Mirco Magnini:** Writing – review & editing, Supervision, Funding acquisition, Conceptualization.

Declaration of competing interest

The authors declare that they have no known competing financial interests or personal relationships that could have appeared to influence the work reported in this paper.

Data availability

The software used to generate the data is publicly available on github and linked to the submission.

Acknowledgements

Appendix A. Mesh sensitivity

The mesh size used for the results presented in Section 4 has a resolution of $160 \times 60 \times 3$ cells along x, y and z respectively. In this appendix, the results of a mesh sensitivity study with four additional grids are shown and reported in Fig. 10. The grids tested in this study are all Cartesian meshes with aspect ratio equal to one along x and y (i.e., $\Delta x = \Delta y$) and have increasing resolution from 100×100 cells up to 240×240. The analysis is run for a coupled simulation performed with $T_{sat} = 0.9$ and $\gamma = 0.2$. The dependence of the numerical solution on the grid spacing is tested for the evolution of vapour mass against time. The results reported in Fig. 10 show that the CFD model exhibits little sensitivity to the mesh resolution in the considered range of grid refinement. Therefore, the choice of the grid with $160 \times 60 \times 3$ cells provides a mesh-independent solution with a relatively low computational cost.

Appendix B. Supplementary content

Supplementary content includes a document outlining additional information about (1) validation of the CFD model and (2) validation of two-way MD-CFD coupling; a video showing the growth of the bubble for MD-only and hybrid MD-CFD simulations is also provided. The video displays the density field obtained with the hybrid framework on the left-hand side, whereas the right-hand side illustrates the corresponding MD-only density field. The hybrid simulation is run with $T_{sat} = 0.9$ and $\gamma = 0.2$.

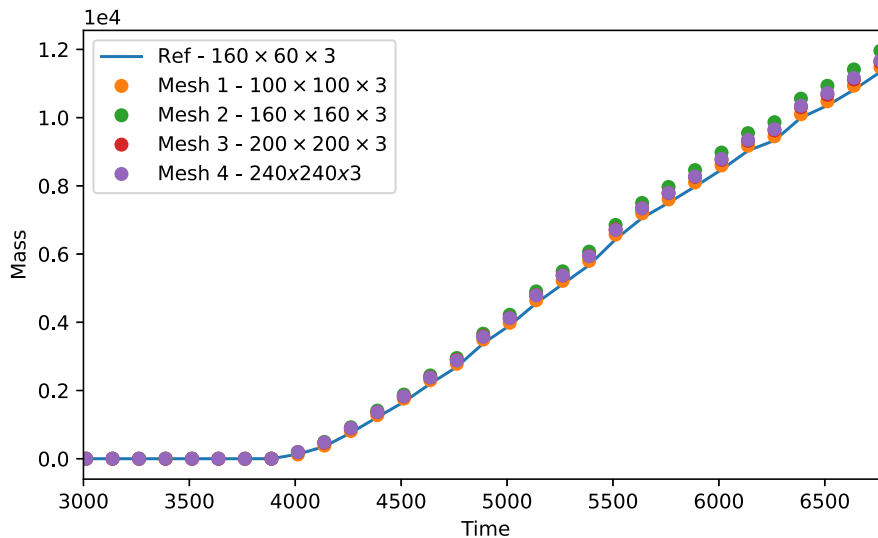Supplementary material related to this article can be found online at https://doi.org/10.1016/j.ijthermalsci.2024.108954.

Fig. 10. CFD mesh sensitivity analysis for the coupled framework. The reference grid uses a vertically elongated cell size ($\Delta y/\Delta x \approx 2.67$), whilst meshes 1–4 have an aspect ratio of one. The reference solution in terms of vapour mass over time is not significantly affected by either decreasing or refining the grid size. The results refer to a coupled simulation run with $T_{sat} = 0.9$ and $\gamma = 0.2$.

References

[1] V.P. Carey, Liquid-Vapor Phase Change Phenomena, Taylor and Francis, 1992.

[2] T.G. Karayiannis, M.M. Mahmoud, Flow boiling in microchannels: Fundamentals and applications, Appl. Therm. Eng. 115 (2017) 1372–1397.

[3] M.M. Mahmoud, T. Karayiannis, Pool boiling review: Part I – Fundamentals of boiling and relation to surface design, Therm. Sci. Eng. Progr. 25 (2021) 101024.

[4] M. Zupancic, P. Gregorcic, M. Bucci, C. Wang, G. Matana Aguiar, M. Bucci, The wall heat flux partitioning during the pool boiling of water on thin metallic foils, Appl. Therm. Eng. 200 (2022) 117638.

[5] A. Kossolapov, B. Phillips, M. Bucci, Can LED lights replace lasers for detailed investigations of boiling phenomena? Int. J. Multiph. Flow 135 (2021) 103522.

[6] A. Richenderfer, A. Kossolapov, J.H. Seong, G. Saccone, E. Demarly, R. Komma-josyula, E. Baglietto, J. Buongiorno, M. Bucci, Investigation of subcooled flow boiling and CHF using high-resolution diagnostics, Exp. Therm. Fluid Sci. 99 (2018) 35–58.

[7] S. Jung, H. Kim, Hydrodynamic formation of a microlayer underneath a boiling bubble, Int. J. Heat Mass Transfer 120 (2018) 1229–1240.

[8] X. Duan, B. Phillips, T. McKrell, J. Buongiorno, Synchronized high-speed video, infrared thermometry, and particle image velocimetry data for validation of interface-tracking simulations of nucleate boiling phenomena, Exp. Heat Transf. 26 (2013) 169–197.

[9] V. Voulgaropoulos, G. Matana Aguiar, C.N. Markides, M. Bucci, Simultaneous laser-induced fluorescence, particle image velocimetry and infrared thermog-raphy for the investigation of the flow and heat transfer characteristics of nucleating vapour bubbles, Int. J. Heat Mass Transfer 187 (2022) 122525.

[10] C. Kunkelmann, P. Stephan, CFD simulation of boiling flows using the volume-of-fluid method within openFOAM, Numer. Heat Transfer, Part A 56 (2009) 631–646.

[11] L. Bures, Y. Sato, Comprehensive simulations of boiling with a resolved microlayer: validation and sensitivity study, J. Fluid Mech. 933 (2022) A54.

[12] A. Urbano, S. Tanguy, G. Huber, C. Colin, Direct numerical simulation of nucleate boiling in micro-layer regime, Int. J. Heat Mass Transfer 123 (2018) 1128–1137.

[13] A. Mukherjee, S.G. Kandlikar, Z.J. Edel, Numerical study of bubble growth and wall heat transfer during flow boiling in a microchannel, Int. J. Heat Mass Transfer 54 (2011) 3702–3718.

[14] M. Magnini, B. Pulvirenti, J.R. Thome, Numerical investigation of hydrodynamics and heat transfer of elongated bubbles during flow boiling in a microchannel, Int. J. Heat Mass Transfer 59 (2013) 451–471.

[15] F. Municchi, I. El Mellas, O.K. Matar, M. Magnini, Conjugate heat transfer effects on flow boiling in microchannels, Int. J. Heat Mass Transfer 195 (2022) 123166.

[16] Y. Sato, B. Niceno, Nucleate pool boiling simulations using the interface tracking method: Boiling regime from discrete bubble to vapor mushroom region, Int. J. Heat Mass Transfer 105 (2017) 505–524.

[17] M. Yazdani, T. Radcliff, M. Soteriou, A.A. Alahyari, A high-fidelity approach towards simulation of pool boiling, Phys. Fluids 28 (2016) 012111.

[18] A.H. Persad, C.A. Ward, Expressions for the evaporation and condensation coefficients in the Hertz-Knudsen relation, Chem. Rev. 116 (2016) 7727–7767.

[19] A.D. Lavino, E. Smith, M. Magnini, O.K. Matar, Surface topography effects on pool boiling via non-equilibrium molecular dynamics simulations, Langmuir 37 (2021) 5731–5744.

[20] A. Shahmardi, O. Tammisola, M. Chinappi, L. Brandt, Effects of surface nanos-tructure and wettability on pool boiling: A molecular dynamics study, Int. J. Therm. Sci. 167 (2021) 106980.

[21] Z.X. Tong, Y.L. He, W.Q. Tao, A review of current progress in multiscale simulations for fluid flow and heat transfer problems: The frameworks, coupling techniques and future perspectives, Int. J. Heat Mass Transfer 137 (2019) 1263–1289.

[22] J. Zhang, M.K. Borg, J.M. Reese, Multiscale simulation of dynamic wetting, Int. J. Heat Mass Transfer 115 (2017) 886–896.

[23] C.W. Hirt, B.D. Nichols, Volume of fluid (VOF) method for the dynamics of free boundaries, J. Comput. Phys. 39 (1981) 201–225.

[24] S.T. O' Connell, P.A. Thompson, Molecular dynamics-continuum hybrid com-putations: a tool for studying complex fluid flows, Phys. Rev. E 52 (1995) R5792.

[25] R. Delgado-Buscalioni, P.V. Coveney, Continuum-particle hybrid coupling for mass, momentum, and energy transfers in unsteady flow, Phys. Rev. E 67 (2003) 046704.

[26] E.R. Fernandez, Modelling Solid/fluid Interactions in Hydrodynamic Flows: A Hybrid Multiscale Approach (Ph.D. thesis), Imperial College London, 2021.

[27] I.A. Cosden, J.R. Lukes, A hybrid atomistic–continuum model for fluid flow using LAMMPS and OpenFOAM, Comput. Phys. Comm. 184 (2013) 1958–1965.

[28] J. Sun, Y. He, W. Tao, X. Yin, H. Wang, Roughness effect on flow and thermal boundaries in microchannel/nanochannel flow using molecular dynamics-continuum hybrid simulation, Comput. Phys. Comm. 184 (2013) 1958–1965.

[29] T.H. Yen, C.Y. Soong, P. Tzeng, Hybrid molecular dynamics-continuum sim-ulation for nano/mesoscale channel flows, Microfluid. Nanofluid. 3 (2007) 665.

[30] N.J. Hadjiconstantinou, Hybrid atomistic-continuum formulations and the moving contact-line problem, J. Comput. Phys. 154 (1999) 245–265.

[31] H.F. Wu, K.A. Fichthorn, A. Borhan, An atomistic-continuum hybrid scheme for numerical simulation of droplet spreading on a solid surface, Heat Mass Trans. 50 (2014) 351–361.

[32] A. Saha, A.K. Das, Multiscale simulation of nanodrop over surfaces with varying hydrophilicity, Comput. Phys. Comm. 294 (2024) 108963.

[33] Y. Mao, B. Zhang, C.L. Chen, Y. Zhang, Hybrid atomistic-continuum simulation of nanostructure defect-induced bubble growth, J. Heat Transfer 139 (2017) 104503.

[34] Z. Liang, T. Biben, P. Keblinksi, Molecular simulation of steady-state evaporation and condensation: Validity of the Schrage relationships, Int. J. Heat Mass Transfer 114 (2017) 105–114.

[35] E.R. Smith, On the Coupling of Molecular Dynamics to Continuum Computational Fluid Dynamics (Ph.D. thesis), Imperial College London, 2014.

[36] E.R. Smith, D.M. Heyes, D. Dini, T.A. Zaki, Control-volume representation of molecular dynamics, Phys. Rev. E. 85 (2012) 056705.

[37] E.R. Smith, E.A. Müller, R.V. Craster, O.K. Matar, A Langevin model for fluctuating contact angle behaviour parametrised using molecular dynamics, Soft Matter 12 (48) (2016) 9604–9615.

[38] E.R. Smith, P.J. Daivis, B.D. Todd, Measuring heat flux beyond Fourier's law, J. Chem. Phys. 150 (6) (2019) 064103.

[39] K. Shi, E.R. Smith, E.E. Santiso, K.E. Gubbins, A perspective on the microscopic pressure (stress) tensor: History, current understanding, and future challenges, J. Chem. Phys. 158 (4) (2023) 040901.

[40] J.H. Irving, J.G. Kirkwood, The Statistical Mechanics Theory of Transport Processes. IV. The Equations of Hydrodynamics, J. Chem. Phys. 18 (1950) 817.

[41] D.J. Evans, G.P. Morriss, Statistical Mechanics of Non-Equilibrium Liquids, second ed., Australian National University Press, Canberra, 2007.

[42] B.D. Todd, P.J. Daivis, Nonequilibrium Molecular Dynamics: Theory, Algorithms and Applications, first ed., Cambridge University Press, Cambridge, 2017, p. 367.

[43] J. Cormier, J.M. Rickman, T.J. Delph, Stress calculation in atomistic simulations of perfect and imperfect solids, J. Appl. Phys. 89 (2001) 99.

[44] F. Municchi, M. Magnini, GitHub repository boilingFoam, 2023, URL https://github.com/fmuni/boilingFoam-PUBLIC.

[45] F. Municchi, C.N. Markides, O.K. Matar, M. Magnini, Computational study of bubble, thin-film dynamics and heat transfer during flow boiling in non-circular microchannels, Appl. Therm. Eng. 238 (2024) 122039.

[46] M. Bucci, Theoretical and Experimental Study of Vapor Bubble Dynamics in Separate Effect Pool Boiling Conditions (Master's thesis), University of Pisa, Pisa, Italy, 2020.

[47] J.U. Brackbill, D.B. Kothe, C. Zemach, A continuum method for modeling surface tension, J. Comput. Phys. 100 (1992) 335–354.

[48] I. Tanasawa, Advances in condensation heat transfer, in: J.P. Hartnett, T.F. Irvine (Eds.), Advances in Heat Transfer, Academic Press, San Diego, 1991.

[49] S. Hardt, F. Wondra, Evaporation model for interfacial flows based on a continuum-field representation of the source terms, J. Comput. Phys. 227 (2008) 5871–5895.

[50] H.G. Weller, A New Approach to VOF-Based Interface Capturing Methods for Incompressible and Compressible Flows, OpenCFD Ltd. Report TR/HGW/04, 2008.

[51] B. van Leer, Towards the ultimate conservative difference scheme. V. A second-order sequel to Godunov's method, J. Comput. Phys. 32 (1979) 101–136.

[52] R.I. Issa, Solution of the implicitly discretized fluid flow equations by operator-splitting, J. Comput. Phys. 62 (1985) 40–65.

[53] N.G. Hadjiconstantinou, A.L. Garcia, M.Z. Bazant, G. He, Statistical error in particle simulations of hydrodynamic phenomena, J. Comput. Phys. 187 (2003) 274–297.

[54] D.A. Lockerby, C.A. Duque-Daza, M.K. Borg, J.M. Reese, Time-step coupling for hybrid simulations of multiscale flows, J. Comput. Phys. 237 (2013) 344–365.

[55] S. Popinet, Numerical models of surface tension, Annu. Rev. Fluid Mech. 50 (2018) 49–75.

[56] E.R. Smith, D.J. Treveljan, E. Ramos-Fernandes, A. Sufian, C. O' Sullivan, D. Dini, CPL library - A minimal framework for coupled particle and continuum simulation, Comput. Phys. Comm. 250 (2020) 107068.

[57] W. Gropp, E. Lusk, A. Skjellum, Using MPI, Third Edition: Portable Parallel Programming with the Message-Passing Interface, MIT Press, 2014.

[58] T. Ishiyama, T. Yano, S. Fujikawa, Molecular dynamics study of kinetic boundary condition at an interface between argon vapor and its condensed phase, Phys. Fluids 16 (2004) 2899–2906.

[59] A. Trokhymchuk, J. Alejandre, Computer simulations of liquid/vapor interface in Lennard-Jones fluids: Some questions and answers, J. Chem. Phys. 111 (1999) 8510–8523.

[60] V.S. Ajaev, G.M. Homsy, Modeling shapes and dynamics of confined bubbles, Annu. Rev. Fluid Mech. 38 (2006) 277–307.

[61] R. Marek, J. Straub, Analysis of the evaporation coefficient and the condensation coefficient of water, Int. J. Heat Mass Transfer 44 (2001) 39–53.

[62] M. Matsumoto, Molecular dynamics of fluid phase change, Fluid Phase Equilib. 144 (1998) 307–314.

[63] J. Wen, D. Dini, H. Hu, E.R. Smith, Molecular droplets vs bubbles: Effect of curvature on surface tension and Tolman length, Phys. Fluids 33 (2021) 072012.

[64] W. Ren, W. E, Heterogeneous multiscale method for the modeling of complex fluids and micro fluidics, J. Comput. Phys. 204 (2005) 1.

[65] E.R. Smith, P.E. Theodorakis, R.V. Craster, O.K. Matar, Moving contact lines: Linking molecular dynamics and continuum-scale modelling, Langmuir 34 (2018) 12501–12518.